



**HAL**  
open science

## **Roles of H<sub>2</sub> evolution overpotential, materials porosity and cathode potential on mineral electro-precipitation in microfluidic reactor -New criterion to predict and assess interdependency**

Faidzul Hakim Adnan, Steve Pontvianne, Marie-Noëlle Pons, Emmanuel Mousset

### ► To cite this version:

Faidzul Hakim Adnan, Steve Pontvianne, Marie-Noëlle Pons, Emmanuel Mousset. Roles of H<sub>2</sub> evolution overpotential, materials porosity and cathode potential on mineral electro-precipitation in microfluidic reactor -New criterion to predict and assess interdependency. *Electrochimica Acta*, 2022, 428, pp.140926. 10.1016/j.electacta.2022.140926 . hal-03842843

**HAL Id: hal-03842843**

**<https://hal.science/hal-03842843>**

Submitted on 7 Nov 2022

**HAL** is a multi-disciplinary open access archive for the deposit and dissemination of scientific research documents, whether they are published or not. The documents may come from teaching and research institutions in France or abroad, or from public or private research centers.

L'archive ouverte pluridisciplinaire **HAL**, est destinée au dépôt et à la diffusion de documents scientifiques de niveau recherche, publiés ou non, émanant des établissements d'enseignement et de recherche français ou étrangers, des laboratoires publics ou privés.

**Roles of H<sub>2</sub> evolution overpotential, materials porosity and cathode potential on mineral electro-precipitation in microfluidic reactor –**

**New criterion to predict and assess interdependency**

Faidzul Hakim ADNAN<sup>1</sup>, Steve PONTVIANNE<sup>1</sup>, Marie-Noëlle PONS<sup>1,2</sup>, Emmanuel MOUSSET<sup>1,\*</sup>

*<sup>1</sup> Université de Lorraine, CNRS, LRGP, F-54000 Nancy, France*

*<sup>2</sup> LTSER-LRGP, CNRS, Université de Lorraine, F-54000 Nancy, France*

**ACCEPTED IN**

***ELECTROCHIMICA ACTA* JOURNAL**

\*Corresponding author. Tel: 0033 372743744; E-mail: [emmanuel.mousset@cnrs.fr](mailto:emmanuel.mousset@cnrs.fr) (Emmanuel Mousset)

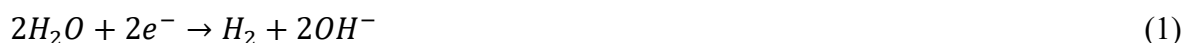
## Abstract

The influence of cathode materials including carbonaceous electrode on the cathodic mineral scaling behavior in a context of wastewater treatment is investigated for the first time and particularly in thin film microfluidic reactors. The kinetics of  $\text{CaCO}_3$  and  $\text{Mg}(\text{OH})_2$  electro-precipitations were evaluated with different cathode materials (with distinct porosities, electroactive surface area ( $S_{\text{elec}}$ ) and hydrogen ( $\text{H}_2$ ) evolution overpotential (HEP)) and by varying the applied current densities and interelectrode distances ( $d_{\text{elec}}$ ). Three electrode materials were tested, carbon paper (porosity = 89%;  $S_{\text{elec}} = 175 \text{ cm}^2$ ), graphite (porosity = 15%;  $S_{\text{elec}} = 85 \text{ cm}^2$ ), stainless steel (porosity = 0%;  $S_{\text{elec}} = 80 \text{ cm}^2$ ). An optimal condition to minimize the mineral deposition could be found in microfluidic configuration ( $100 \mu\text{m } d_{\text{elec}}$ ) and by using graphite material being able to increase cathodic potential ( $E_C$ ) so to decrease  $\text{OH}^-$  production. At higher  $d_{\text{elec}}$ , stainless steel led to less electro-precipitation compared with graphite. These results newly highlight that the electro-precipitation rate strongly depends on  $E_C$  values, which vary with current density and  $d_{\text{elec}}$ , as well as with the materials properties (porosity,  $S_{\text{elec}}$ , HEP). A new criterion, namely  $E_C/\text{HEP}$ , has been introduced to assess the interdependency of those parameters. Interestingly, a maximal electro-precipitation was noticed at  $E_C/\text{HEP} \approx 1.3$  for porous and non-porous materials. This further announces the possibility to predict the range of required  $E_C$  according to the electro-precipitation objective, which is crucial in real applications of electrolysis for wastewater treatment.

**Keywords:** Electro-oxidation; Impedance spectroscopy; Inter-electrode distance; Scaling issue; Wastewater treatment

## 1. Introduction

Carbonaceous materials such as carbon felt, graphite felt and carbon sponge are well-known to inherit high porosity features that can overcome mass transport limitation owing to their great specific surface [1]. They have also been the subject of research due to their high electrocatalytic properties, while offering low operating cost and environmentally-friendly properties compared to noble metals [2]. This can benefit wide ranges of prospective applications [1, 3, 4], including water treatment domain [5, 6]. Besides, another distinct characteristic of carbonaceous materials is that they possess lower overpotential for water reduction [7]. Consequently, wider potential window under cathodic range is achieved, prior to hydrogen evolution reaction (HER) (Eq. 1) [3]:



This interesting feature permits the electrogeneration of hydrogen peroxide ( $H_2O_2$ ) from 2-electron oxygen ( $O_2$ ) reduction reaction (ORR) (Eq. 2) [8-10]:



$H_2O_2$  is the main reagent involved in the Fenton reaction that produces hydroxyl radical ( $\bullet OH$ ) in the emerging electrochemical advanced oxidation processes (EAOPs), particularly in electro-Fenton systems [11, 12].  $\bullet OH$  is then responsible for the high removal rates and yields obtained with biorecalcitrant organic pollutants present in wastewater [13-15]. EAOPs have demonstrated to be highly efficient to deal with large range of organic load in effluents to treat [16, 17]. However, calcium ( $Ca^{2+}$ ), carbonates ( $HCO_3^-/CO_3^{2-}$ ), and in a lesser extent magnesium ( $Mg^{2+}$ ), are frequently found in real effluents [18-24]. They entail an additional treatment constraint (e.g., polarity reversal) which has barely been taken into account in EAOPs applications until now. These ions precipitate on the cathode surface due to local alkalization (Eqs. 1 and 3), a phenomenon involved during electrolysis of aqueous solution [25-27].



The accumulation of non-conducting precipitates induces a mineral scaling on the cathode that passivates it over the course of electrolysis.

The use of microfluidic reactors in the field of water treatment has been proven promising owing to mass transfer promotion, reduction in specific power consumption whilst allowing to treat waste effluents possessing low electrical conductivity [28-35]. However, the influence of hydrogen evolution potential and more generally of the carbon-based materials compared to metal cathode on the cathodic scaling is still questioned in such microfluidic setup and has never been elucidated yet.

Therefore, this article investigates in detail for the first time the influence of the properties of carbonaceous materials on the occurrence of cathodic passivation during the advanced electro-oxidation treatment of simulated wastewater effluent. The cathode materials were firstly characterized using an electrochemical method before being subjected to electrolysis at different applied current densities. The role of electrode porosity was particularly explored and the amount of mineral electro-precipitation produced was systematically quantified. The role of overpotential for H<sub>2</sub> evolution on the kinetics of electro-precipitation was further examined. The synergistic effect of HEP coupled with the electrochemical configuration was discussed. The comparison between the occurrence of mineral scaling on different cathode materials inside submillimetric and millimetric interelectrode distance ( $d_{\text{elec}}$ ) was also evaluated. Moreover, the new insights given by mechanistic understanding towards the electrochemical and chemical processes taking place at the electrode/electrolyte interface was substantiated with the *in-situ* electrochemical impedance analysis. Finally, a new criterion is proposed to predict the optimal range of cathode potential ( $E_C$ ) to apply as a function of electro-precipitation goal and at a given material.

## 2. Experimental

### 2.1. Chemicals

Calcium sulfate dihydrate (> 90%), magnesium sulfate heptahydrate (> 98%), sodium hydrogenocarbonate (> 99.5%) and sodium sulfate (> 97%) were provided by VWR International (Fontenay-sous-Bois, France). Sulfuric acid (95-97%) was purchased from Sigma Aldrich (Saint-Quentin-Fallavier, France). Sodium hydroxide (1 N) was obtained by Honeywell Fluka (Seelze, Germany). These chemical reagents were used without further purification. A PureLab ELGA Classic water purification system (Veolia Water, Antony, France) was used to provide ultrapure water (18.2 M $\Omega$  cm).

### 2.2. Electrolysis setup

Galvanostatic electrolysis using flow-by parallel-plate configuration was used to run the electrolysis according to a setup detailed elsewhere [27, 36]. Two values of applied current were investigated: 20 (0.4 mA cm<sup>-2</sup>) and 200 mA (4 mA cm<sup>-2</sup>) using a HMP4040 power supply (Rohde & Schwarz, Meudon-la-Forêt, France). BDD served as anode, while 316L stainless steel (Gantois Industries, Saint-Dié-des-Vosges, France), graphite plate (Final Advanced Materials, Didenheim, France) or carbon paper GDL 39AA (Ion Power, München, Germany) (280  $\mu$ m thickness, no polytetrafluoroethylene (PTFE) treatment) was used as cathode. During the study of the role of interelectrode gap, three  $d_{\text{elec}}$  were investigated: 100 and 500  $\mu$ m, representing submillimetric configurations, and 3000  $\mu$ m representing the millimetric scale. The electrolysis was carried out using 500 mL solution containing 150 mg L<sup>-1</sup> Ca<sup>2+</sup>, 5 mg L<sup>-1</sup> Mg<sup>2+</sup> and 60 mg-C L<sup>-1</sup> of total inorganic carbon (TIC), which was representative of the properties of reclaimed municipal wastewater [27]. The solutions were recirculated at flow rates of 20, 100 and 600 mL min<sup>-1</sup> using 100, 500 and 3000  $\mu$ m  $d_{\text{elec}}$  respectively, to ensure an equivalent residence time (0.025 min) under each condition, while staying under similar hydrodynamic regime (laminar) [36].

### 2.3. Analytical and characterization methods

Cyclic voltammetry (CV) was performed in a three-electrode configuration [37] to estimate the  $S_{\text{elec}}$  of the different cathode materials under study using a potentiostat (Ametek, Massy, France) [38, 39]. 500 mL of solution containing 50 mM of  $\text{K}_4\text{Fe}(\text{CN})_6$  in 0.50 M of  $\text{Na}_2\text{CO}_3$  was used [38, 39]. The cathode material to be characterized was used as working electrode (WE), BDD was the counter electrode (CE) and Ag-AgCl was the reference electrode (REF). The potential was swept between 0.6 and -0.8 V/Ag-AgCl with a scan rate of  $10 \text{ mV s}^{-1}$ . Interelectrode gap of  $500 \mu\text{m}$  was implemented during this characterization experiments. The electrolyte was circulated at  $100 \text{ mL min}^{-1}$ .

To determine the exchanged current ( $I_0$ ) of cathode materials, linear sweep voltammetry (LSV) was performed using the electrolyte ascribed in Section 2.2 [40]. A potential sweep between 0.5 and -1.8 V/Ag-AgCl with  $10 \text{ mV s}^{-1}$  scan rate was conducted. Stainless steel, graphite and carbon paper were used as the WE, BDD as CE and Ag-AgCl as REF.

Electrochemical impedance spectroscopy (EIS) was conducted in galvanostatic mode in frequencies ranging between 100 kHz to 100 mHz to characterize the electrochemical behavior of electrolyte at the interface of the investigated cathodes during electrolysis (i.e., charge transfer resistance ( $R_{\text{CT}}$ ), double layer capacitance ( $C_{\text{DL}}$ ), resistance of porous non-conductive precipitation film ( $R_{\text{F}}$ )), by following the protocol and the equivalent electrical circuit model defined in a previous study [36].

Inductively coupled plasma optical emission spectroscopy ICP-OES (Thermo iCAP 6000, Thermo Fisher, Noisy-Le-Grand, France) was used to quantify Mg and Ca concentrations, while the evolution of TIC concentration was followed using a TOC-TN analyzer (Shimadzu  $\text{V}_{\text{CSH}}$ , Marne-La-Vallée, France) as described previously [36].

### 3. Results and discussions

#### 3.1. Influence of the porosity of cathode material on the formation of electro-precipitate

##### 3.1.1. Electroactivity of stainless steel, graphite and carbon paper characterized by electrochemical method

Redox reactions of  $\text{Fe}(\text{CN}_6)^{3-}$  and  $\text{Fe}(\text{CN}_6)^{4-}$  were used to estimate the electroactivity of the three investigated cathode surfaces. **Figure 1** illustrates the CV obtained with stainless steel, graphite and carbon paper. The peak current ( $I_P$  in A) is correlated to the  $S_{\text{elec}}$  of an electrode by Randles-Sevcik equation (**Eq. 4**) [38, 39, 41]:

$$I_P = 2.69 \times 10^5 \times AD_L^{1/2} n_e^{3/2} \gamma^{1/2} C_{\text{SOL}} \quad (4)$$

where  $A$  is the  $S_{\text{elec}}$  (in  $\text{cm}^2$ ),  $D_L$  is the diffusion coefficient of  $\text{Fe}(\text{CN}_6)^{3-}/\text{Fe}(\text{CN}_6)^{4-}$  in solution ( $6.48 \times 10^{-6} \text{ cm}^2 \text{ s}^{-1}$  [42-44]),  $n_e$  equals to 1,  $\gamma$  is the scan rate ( $0.01 \text{ V s}^{-1}$ ) and  $C_{\text{SOL}}$  is  $5 \times 10^{-5} \text{ mol cm}^{-3}$ .

From the values of  $I_P$  measured for the three cathode materials (**Fig. 1**), their corresponding values of  $S_{\text{elec}}$  were determined. It was estimated that the stainless steel (**Fig. 1(a)**), graphite (**Fig. 1(b)**) and carbon paper (**Fig. 1(c)**) possessed 80, 85 and 175  $\text{cm}^2$  of surface area, respectively. This trend is coherent with the increase of electrode porosity from stainless steel to graphite (~15%, Final Advanced Materials, Didenham, France) and carbon paper (~89%, Ion Power, München, Germany). There was only 6% difference between graphite and stainless steel despite the former being a carbonaceous material. This slightly higher  $S_{\text{elec}}$  of graphite was due to the fact that both stainless steel and graphite used in this work were solid plate electrodes. Porous properties of graphite gave slight advantage compared to stainless steel plate. Significant increase of  $S_{\text{elec}}$  was provided by the carbon paper as expected. It was attributed to its high porosity which increased the number of electroactive sites at the cathode interface.

The LSV and the respective Tafel slopes of the three investigated cathode materials in synthetic effluent (150 mg L<sup>-1</sup> Ca<sup>2+</sup>, 5 mg L<sup>-1</sup> Mg<sup>2+</sup> and 60 mg-C L<sup>-1</sup> of TIC) used to study the formation of electro-precipitation are given in **Fig. 2**. From the Tafel slopes, the exchanged current ( $I_0$ ) on stainless steel, graphite and carbon paper were estimated to be 1.2, 7.9 and 15.8 mA, respectively.  $I_0$  indicated the easiness of electrons transfer that could occur at the electrode/electrolyte interface. From the values of  $I_0$ , the charge transfer resistance ( $R_{CT}$ ) could hence be estimated using **Eq. 5** [45, 46]:

$$R_{CT} = \frac{RT}{n_e F I_0} \quad (5)$$

where  $R_{CT}$  is in  $\Omega$ ,  $R$  is the gas constant (8.314),  $T$  is the temperature (in K) and  $n_e$  is the number of exchanged electrons for water reduction. Here,  $n_e$  equals to 2, due to the fact that water reduction by two electrons was the dominant faradaic reaction at the applied current investigated [27].

By intermediary of **Eq. 5**,  $R_{CT}$  on stainless steel, graphite and carbon paper were estimated to be 10.2, 1.62 and 0.81  $\Omega$ , respectively. These numbers foretell that electronic transfer is the easiest on carbon paper, followed by graphite and finally on stainless steel cathode. It tallies with the respective order of the above-mentioned surface of materials. The values of  $R_{CT}$  are compared with those measured with another technique (i.e., EIS) in **Section 3.2.2**.

In the meantime, the role of cathode material on the kinetics of electro-precipitation during the electrolysis of solution containing 150 mg L<sup>-1</sup> Ca<sup>2+</sup>, 5 mg L<sup>-1</sup> Mg<sup>2+</sup> and 60 mg-C L<sup>-1</sup> of TIC is scrutinized in the next section.

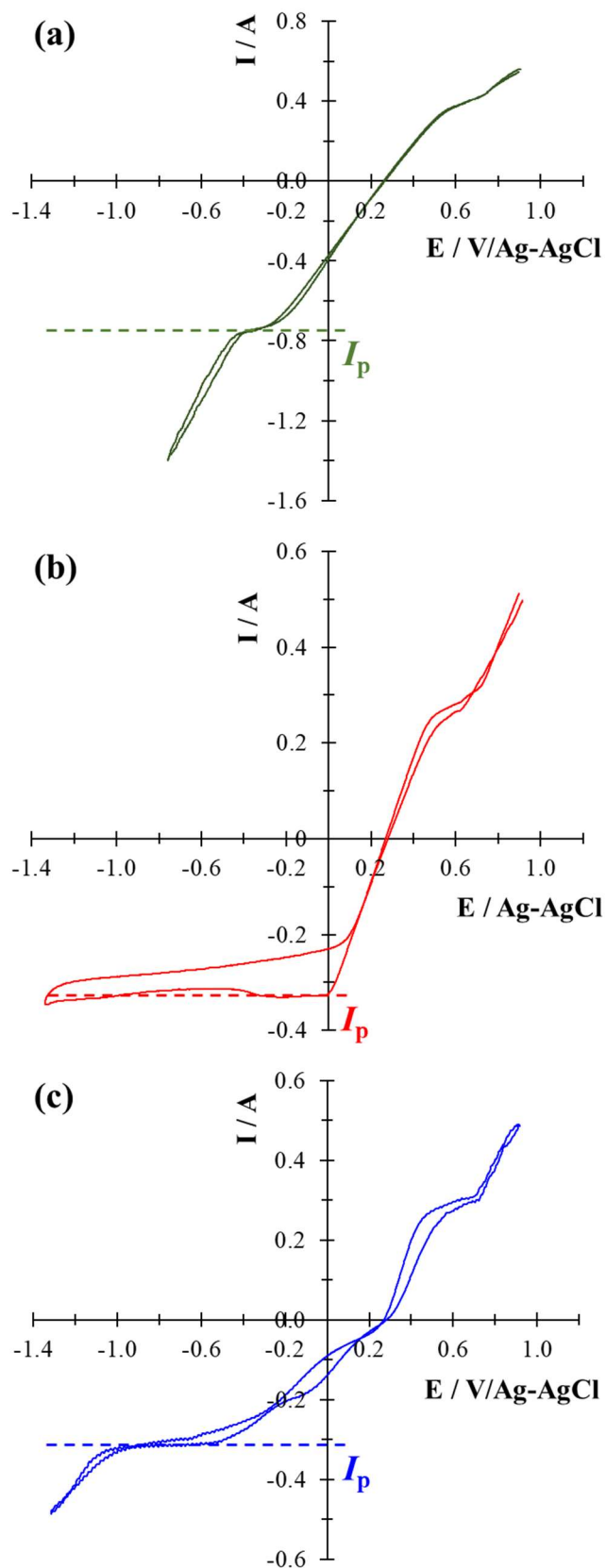


**Fig. 1.** CV on (a) carbon paper, (b) graphite and (c) stainless steel for the determination of  $S_{elec}$ . Electrolyte: 500 mL of 50 mM of  $K_4Fe(CN)_6$  in 0.50 M of  $Na_2CO_3$ ; potential sweep between 0.6 to -1.6 V/Ag-AgCl with a scan rate of  $10 \text{ mV s}^{-1}$ ; CE: BDD, REF: Ag-AgCl and  $d_{elec}$ : 500  $\mu\text{m}$ .

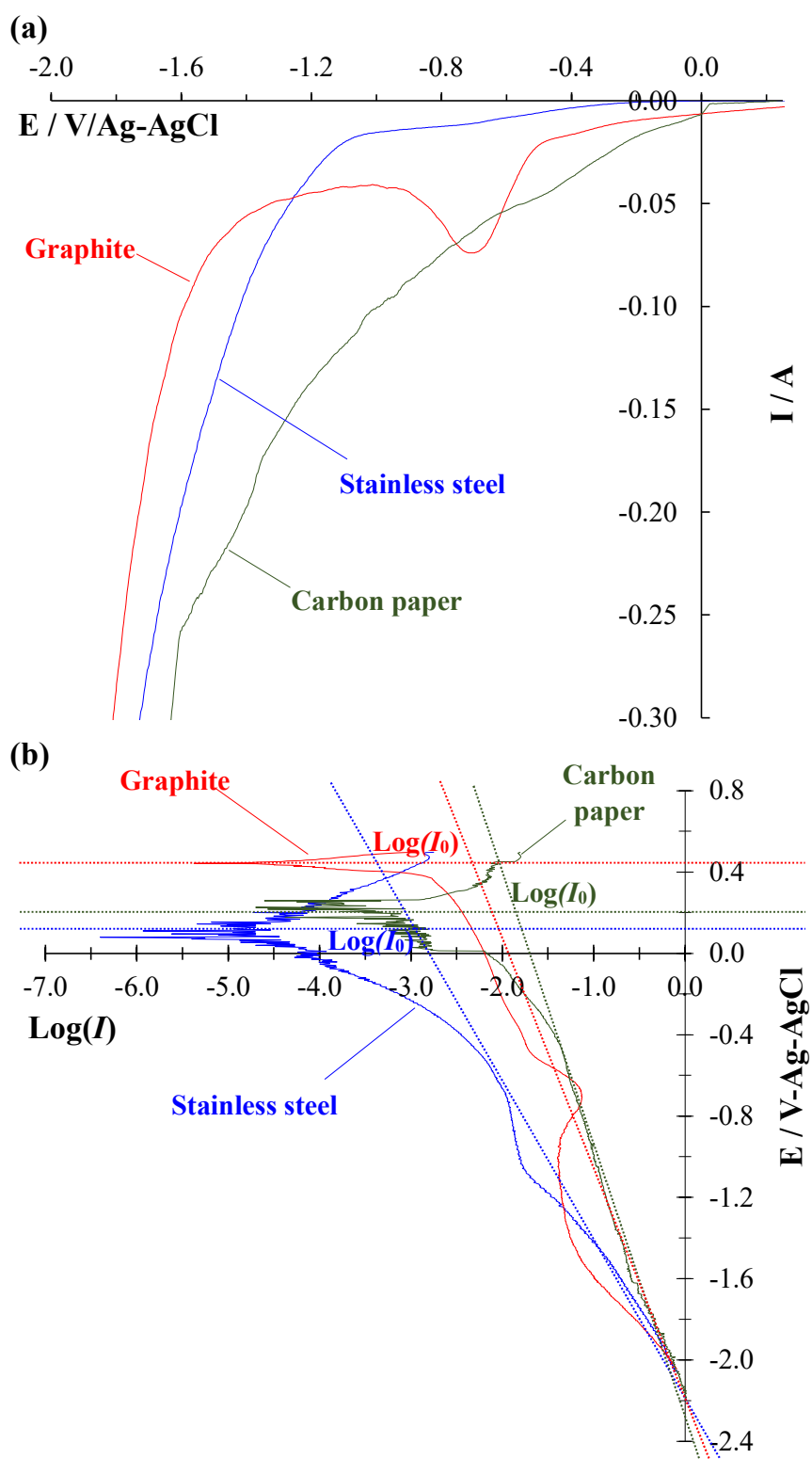


**Fig. 2.** LSV (a) and respective Tafel slopes (b) of stainless steel, graphite and carbon paper for the estimation of  $I_0$ . 500 mL solution containing  $150 \text{ mg L}^{-1} \text{ Ca}^{2+}$ ,  $5 \text{ mg L}^{-1} \text{ Mg}^{2+}$  and  $60 \text{ mg-C L}^{-1}$  of TIC. Potential sweeps between 0.5 to -1.8 V/Ag-AgCl with a scan rate of  $10 \text{ mV s}^{-1}$ ; CE: BDD, REF: Ag-AgCl and  $d_{\text{elec}}$ :  $500 \text{ }\mu\text{m}$ .

### 3.1.2. Electro-precipitation on different cathode materials at various applied current densities

In this section, the formation of electro-precipitate occurring on stainless steel, graphite and carbon paper under the polarization of different applied currents was evaluated. **Figure 3** illustrates some photographs of mineral electro-precipitate that were formed on the investigated cathodes polarized at 200 mA. The scaling appeared whitish on stainless steel (**Fig. 3(a)**) and graphite (**Fig. 3(b)**), whereas the white appearance was not seen on carbon paper (**Figs. 3(c)-3(d)**). Perhaps, the electro-precipitation took place within the pores using carbon paper. With the occurrence of mineral scaling being proven, its quantitative analysis on different cathode materials and applied current was conducted. The evolution of  $Mg^{2+}$ ,  $Ca^{2+}$  and TIC concentrations during the 5 h of electrolysis at 20 and 200 mA are plotted in **Fig. 4**. In **Fig. 4(a)**,  $Mg^{2+}$  concentration decreased insignificantly for all three investigated cathode materials when 20 mA was applied.  $Mg^{2+}$  concentration decreased by  $5.2 \pm 0.1\%$  using stainless steel and by 7% using graphite. Meanwhile, using carbon paper,  $Mg^{2+}$  concentration dropped by 2.1% after 3 h electrolysis before it re-dissolved into the solution, which could be in relation with the porous nature of the cathode, the microfluidic configuration and the pH evolution as explained later in this sub-section. From these results, it could be deduced that little  $Mg(OH)_2$  precipitation occurred on all cathode materials investigated at low applied current. With respect to the evolution of  $Ca^{2+}$  concentration at 20 mA as shown in **Fig. 4(c)**, it decreased indifferently when stainless steel and graphite cathodes were used considering the standard deviations. It decreased to  $45.8 \pm 3.3\%$  and to  $47.8 \pm 1.0\%$  using stainless steel and graphite, respectively. The evolution of  $Ca^{2+}$  followed a similar trend as the evolution of  $Mg^{2+}$  in the case of carbon paper.  $Ca^{2+}$  concentration dropped by  $11.2 \pm 0.8\%$  after 3 h of electrolysis before dissolving back into solution to yield only 1.3% of Ca precipitation on carbon paper at the end of electrolysis. The evolution of TIC concentration is given in **Fig. 4(e)**. Their evolutions followed those of  $Ca^{2+}$  plotted in **Fig. 4(c)** with the exception of carbon paper. It was observed that TIC was depleted after 5 h of electrolysis:  $90 \pm 18\%$ ,  $94 \pm 14\%$  and  $94 \pm 7\%$  of carbonates loss in the setup using stainless

steel, graphite and carbon paper, respectively. Using stainless steel and graphite, the decrease of carbonates in conjunction with  $\text{Ca}^{2+}$  concentration confirmed the  $\text{CaCO}_3$  electro-precipitation on both cathodes. Contrastingly, using carbon paper polarized at 20 mA, the TIC in the solution was depleted but  $\text{Ca}^{2+}$  only precipitated by 1.3% at the end of electrolysis. Therefore,  $\text{HCO}_3^-/\text{CO}_3^{2-}$  might loss via an additional route, which is discussed later in this sub-section.

The evolution of  $\text{Mg}^{2+}$ ,  $\text{Ca}^{2+}$  and TIC concentrations on stainless steel, graphite and carbon paper at higher applied current (200 mA) are shown in **Figs. 4(b)**, **4(d)** and **4(f)**, respectively. From **Fig. 4(b)**, it was observed that a similar degree of precipitation of  $\text{Mg}^{2+}$  was achieved on the surface of stainless steel and graphite ( $91.0 \pm 1.8\%$  and  $89.1 \pm 2.2\%$ , respectively). In contrast, lower  $\text{Mg}^{2+}$  precipitation was observed on carbon paper (i.e.  $20.2 \pm 1.1\%$ ). With regard to the evolution of  $\text{Ca}^{2+}$  concentration at 200 mA (**Fig. 4(d)**),  $\text{Ca}^{2+}$  precipitated by  $43.2 \pm 5.6\%$  and  $46.7 \pm 1.2\%$  after 5 h of electrolysis when stainless steel and graphite were used as cathode, respectively. Thus, 3.5% more  $\text{CaCO}_3$  precipitated on graphite in comparison to stainless steel. When carbon paper was adopted as cathode,  $\text{Ca}^{2+}$  precipitated by  $48.2 \pm 1.3\%$  after just only 1 h of electrolysis. However, the precipitate re-dissolved into the bulk after 1 h of treatment and it ended with  $40.0 \pm 1.5\%$  of  $\text{Ca}^{2+}$  precipitation, which was less than on stainless steel and graphite. **Figure 4(f)** plots the evolution of TIC using the three cathode materials under the polarization of 200 mA. Comparable trends seen in the cases with 20 mA were observed. More precipitation of carbonates occurred using the graphite cathode setup ( $95.8 \pm 5.4\%$ ) versus the stainless steel ( $89.4 \pm 0.2\%$ ). This corroborated with the evolution of  $\text{Ca}^{2+}$  concentration where slightly more  $\text{Ca}^{2+}$  precipitated on graphite relatively to stainless steel. Regarding the TIC evolution under the carbon paper setup, as it was the case with  $\text{Ca}^{2+}$ , TIC depleted quickly down to  $94.6 \pm 0.9\%$  just after 1 h of electrolysis. TIC decreased significantly faster at higher applied current in comparison to the case where 20 mA was applied (i.e., 4 h to deplete the TIC by 94% (**Fig. 4(e)**)).

The peculiarity of the results obtained when carbon paper was used as cathode at both applied currents could be justified by the trend of electrolytic solution pH over the course of electrolysis. **Figure 5** plots the variation of electrolyte pH in the bulk at both applied current investigated. It was observed that the bulk pH decreased the most using carbon paper as cathode regardless of applied current. Under the polarization of 20 mA using carbon paper (**Fig. 5(a)**), the bulk pH decreased to an average pH value of 5.12 before it dropped to 3.38 after 4 h and further down to 3.12 after 5 h of electrolysis. This explained why there was a re-dissolution of Mg and Ca precipitates starting from 3 h of electrolysis onwards in the case of 20 mA. Regarding the pH evolution at higher applied current (**Fig. 5(b)**), it dropped rapidly to 3.76 after just 1 h of electrolysis, before settling at 3.56 at the end of the process. Similarly, this could explain the re-dissolution of Ca as well as the quicker depletion of TIC after 1 h of electrolysis when 200 mA was applied. From these trends of bulk pH, it could be summarized that the carbonate loss in case of carbon paper was principally due to the conversion of  $\text{HCO}_3^-$  to  $\text{H}_2\text{CO}_3$  ( $\text{pK}_A = 6.3$  [47]) and then to  $\text{CO}_2$  given the low pH environment ( $\text{pH} = 3.56$ ) obtained using carbon paper. This was particularly true in the case of 20 mA where TIC was depleted by 94% but  $\text{Ca}^{2+}$  only precipitated by 11% (before re-dissolution). While applying 200 mA,  $\text{Ca}^{2+}$  quickly precipitated with  $\text{CO}_3^{2-}$  during the first hour of electrolysis before the pH environment got too low that it induced re-dissolution of  $\text{CaCO}_3$  after 1 h electrolysis.

Moreover, the bulk pH tends to stabilize towards the end of electrolysis with carbon paper (**Fig. 5**), and quicker stabilization was observed with higher current density (**Fig. 5(b)**). This could be explained by the progressive accumulation of  $\text{H}^+$  from the anode in the porous cathode due to microfluidic configuration (500  $\mu\text{m}$ ), which then redissolve the precipitates into the bulk as noticed in **Figs. 4**. This phenomenon of redissolution starts earlier at higher current density (after 60 min at 200 mA against 240 min at 20 mA), due to higher accumulation of  $\text{H}^+$  at anode, which agreed with the stabilization of pH in the bulk after 240 min at 20 mA and 60 min at 200 mA (**Fig. 5**). The re-dissolution mechanisms were not observed with graphite and stainless steel cathodes, because it was assumed that the  $\text{H}^+$  did not have time to accumulate at the cathode surface in order to compensate

the OH<sup>-</sup> production, due to their too low porosity. Furthermore, a fluctuation of results with higher standard deviation during electrolysis with carbon paper was evidenced. It could be attributed to the changes of electro-precipitation kinetics with the anodic contribution in microfluidic design that decrease the reproducibility.

The evolution of bulk pH when stainless steel and graphite were used as cathode are also depicted in **Fig. 5**. It can be observed that, regardless of the value of applied current, the electrolytic bulk pH decreased in the increasing order of stainless steel > graphite > carbon paper. Comparing the porosity of the three cathode materials, it increased in the increasing order of stainless steel < graphite < carbon paper. This observation concludes the effect of porosity on the formation of cathodic deposition. Porous nature of the electrode would induce a retardation of OH<sup>-</sup> diffusion flux from the pores into the solution bulk [48]. As a consequence, more accumulation of OH<sup>-</sup> occurred in the pores due to the slower OH<sup>-</sup> diffusion which led to higher local pH on porous cathode. In the same time, the precipitation reactions near the cathode surface consumed OH<sup>-</sup> [49, 50]. This consumption of OH<sup>-</sup> combined with its slower diffusion into the bulk could have led to higher uncombined H<sup>+</sup> concentration in the bulk, which resulted in lower bulk pH value. This could be the reason why lower bulk pH was obtained using carbon paper as cathode, followed by graphite and stainless steel. Therefore, carbon paper which had highest porosity could have led to the highest accumulation of OH<sup>-</sup>, which could then rapidly convert HCO<sub>3</sub><sup>-</sup> into CO<sub>3</sub><sup>2-</sup> for its reaction with Ca<sup>2+</sup> to form CaCO<sub>3</sub> (**Fig. 4(d)**). Following similar principles, the porous nature of graphite plate led to slightly higher local OH<sup>-</sup> concentration on graphite cathode relatively to the stainless steel plate which resulted in slightly higher CaCO<sub>3</sub> electro-precipitation on graphite as compared to stainless steel (**Figs. 4(d)** and **4(f)**).

It is also interesting to link the hydrophobicity of the cathode material with the occurring electro-precipitation. The increase of contact angles values from stainless steel (73°; [51]) to graphite (78°; [39]) and carbon paper (~150°, according to a similar carbon paper characteristic (280 μm, no PTFE

treatment, 80% of porosity; [52]), highlights the increase of hydrophobicity with the increasing cathodic electro-precipitation. This could be explained by the increase of O<sub>2</sub> gas affinity towards the most hydrophobic material (i.e., carbon paper), which then increases the possibility of its subsequent reduction that lead to higher OH<sup>-</sup> generation. This O<sub>2</sub> is preferentially transferred from anode to cathode in microfluidic device.

The only exception on the kinetics trend of electro-precipitation was the case when carbon paper was used as cathode under the polarization of 20 mA. The sluggish kinetics of CaCO<sub>3</sub> precipitation were attributed to the high applied  $E_C$  on carbon paper. It was measured at -0.35 V/Ag-AgCl using 20 mA and this potential was too high for the either reduction of O<sub>2</sub> or water to occur [25, 26, 36]. As a result, OH<sup>-</sup> was not yet produced. Slow electro-precipitation of Mg(OH)<sub>2</sub> on carbon paper in comparison to graphite and stainless steel using 200 mA current was also due to similar reason. It has been shown in literature that the precipitation of Mg(OH)<sub>2</sub> was highly dependent on applied current [21, 53-55], or more precisely to the  $E_C$  [27]. When 200 mA was applied,  $E_C$  of -1.54 V/Ag-AgCl was measured on stainless steel, -1.72 V/Ag-AgCl was measured on graphite, whilst relatively higher -1.40 V/Ag-AgCl was measured on carbon paper (Fig. 2). This higher applied  $E_C$  led to lower intensity of OH<sup>-</sup> production from the reduction reactions of water (Eq. (1)) and dissolved O<sub>2</sub> (Eq. (3)). Hence, slower Mg(OH)<sub>2</sub> electro-precipitation was apparent with carbon paper.

Due to the difference of electro-precipitation behavior obtained with regard to cathode materials, the influence of H<sub>2</sub> evolution potential was further scrutinized in the next section.



**Fig. 3.** Photographs of mineral electro-precipitation occurring on **(a)** stainless steel, **(b)** graphite and **(c, d)** carbon paper cathodes after 5 h electrolysis.  $d_{\text{elec}}$ : 500  $\mu\text{m}$ .  $I_{\text{app}}$ : 200 mA.

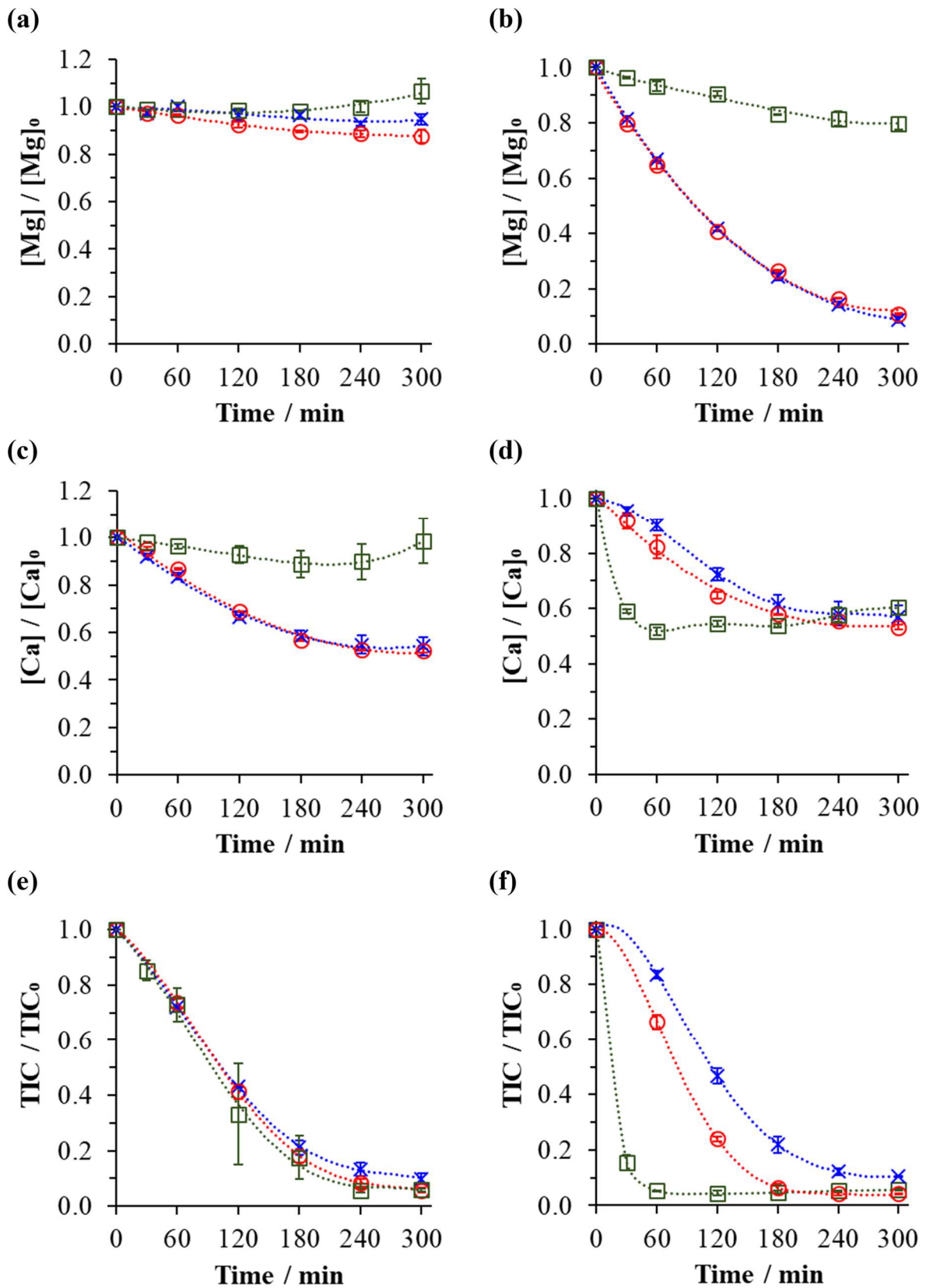


**Fig. 4.** Concentrations of  $\text{Mg}^{2+}$ ,  $\text{Ca}^{2+}$  and TIC during the electrolysis at 20 mA ((a), (c), (e)) and 200 mA ((b), (d), (f)).  $d_{\text{elec}}$ : 500  $\mu\text{m}$ , (x): stainless steel, (o): graphite and (□): carbon paper cathode.

Electrolyte initially contained 150  $\text{mg L}^{-1}$   $\text{Ca}^{2+}$ , 5  $\text{mg L}^{-1}$   $\text{Mg}^{2+}$  and 60  $\text{mg-C L}^{-1}$  of TIC.

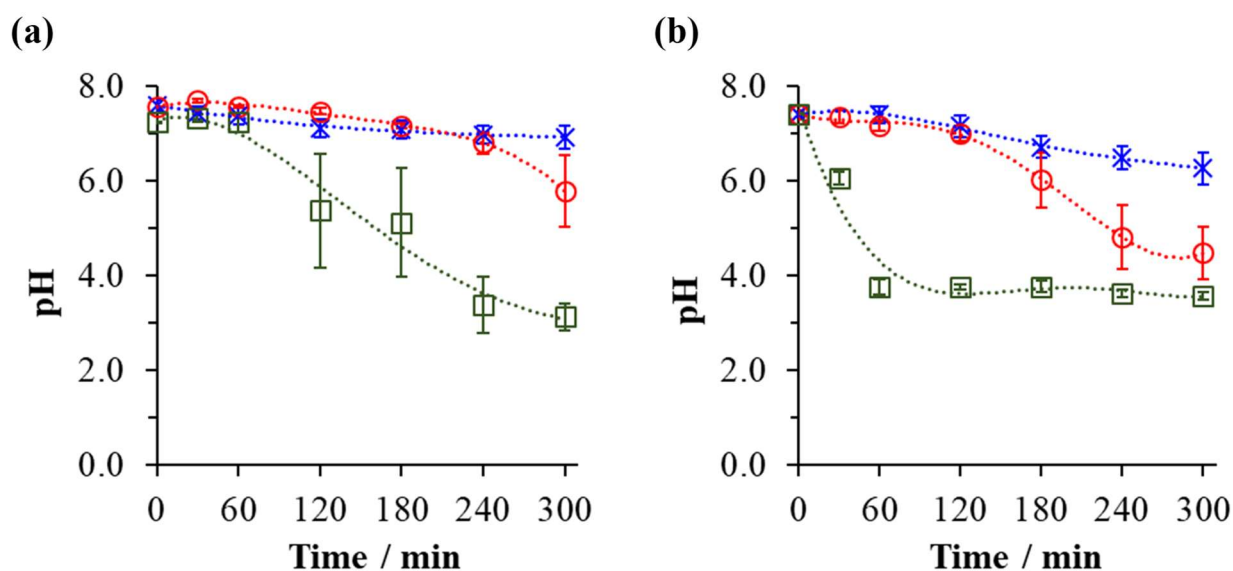


**Fig. 5.** Evolution of bulk pH during the electrolysis at **(a)** 20 mA and **(b)** 200 mA. Cathode material: (**x**): stainless steel, (**o**): graphite and (**□**): carbon paper.

### 3.2. Role of H<sub>2</sub> evolution overpotential: synergistic effect of interelectrode distance and cathode material to reduce electro-precipitation

It has been demonstrated across [Section 3.1](#) that by using more porous cathodes, it works in favor of mineral electro-precipitation. It corroborates the fact that a porous cathode offers high  $S_{elec}$ , which enhances chemical and electrochemical reactions. As a consequence, if the formation of electro-precipitation is intended, porous cathode is the go-to option. Contrastingly, if the depreciation of mineral electro-precipitation is sought after, which is rather the case with the EAOPs in order to increase their life span, using cathodes with high porosity might yield antagonistic consequences.

In this section, another property of carbonaceous material has been explored. Carbonaceous material such as carbon felt, graphite felt, vitreous carbon and graphite rod are known to possess higher overpotential for water reduction [\[39\]](#). Consequently, a wider potential window under cathodic range prior to H<sub>2</sub> evolution is achieved. That is the reason why carbonaceous materials have been receiving specific attention for a variety of applications (e.g. Fenton-based technology [\[56-60\]](#), non-Fenton catalytic degradation of organics [\[61, 62\]](#), electrosorption [\[63\]](#) as well as fuel cells and batteries [\[3,](#)

64, 65]) benefiting both their lower cost and environmentally-friendly properties. Moreover, it has been previously shown that the electro-precipitation occurs with concomitant HER [53, 55, 66-68] which results in deposit detachment from cathode surface [55, 67, 69, 70]. In that regards, carbonaceous cathode is of no exemption. Due to the determinant role of concurrent gas evolution on electro-precipitation formation, the overpotential of H<sub>2</sub> evolution offered by a carbonaceous material was further explored (Section 3.2.1). Graphite plate, a low porosity carbonaceous electrode (~15%) was used as cathode to meet the objective. The kinetics of electro-precipitation taking place on graphite together with stainless steel plate were compared under both submillimetric and millimetric configurations to inspect the inter-relation between interelectrode gap and H<sub>2</sub> overpotential. The mechanistic understanding at the cathode/electrolyte interface is further deepened through electrochemical impedance analysis presented in Section 3.2.2. The introduction of a new criterion assessing electro-precipitation efficiency considering  $E_C$  and HEP as a function of material porosity is exposed in Section 3.2.3.

### 3.2.1. Electro-precipitation on stainless steel and graphite at different interelectrode distances

Figure 6 shows the evolution of Mg<sup>2+</sup>, Ca<sup>2+</sup> and TIC deposited during the electrolysis at 200 mA, when either graphite or stainless steel plates were used as cathode. From the plot of Mg<sup>2+</sup> concentration evolution in Fig. 6(a), it was observed that more Mg<sup>2+</sup> electro-precipitated using 500  $\mu\text{m}$   $d_{\text{elec}}$  in comparison with 3000  $\mu\text{m}$  setup. Using 500  $\mu\text{m}$ , comparable Mg<sup>2+</sup> electro-precipitation was noticed between stainless steel ( $91.0 \pm 1.8\%$ ) and graphite ( $89.1 \pm 2.2\%$ ). When  $d_{\text{elec}} = 3000$   $\mu\text{m}$ , Mg<sup>2+</sup> precipitated by  $81.1 \pm 0.2\%$  and  $82.6 \pm 2.8\%$  on stainless steel and graphite, respectively. Under the 100  $\mu\text{m}$  setup, a different behavior was noticed.  $85.6 \pm 2.6\%$  of Mg<sup>2+</sup> precipitated on stainless steel which was comparable to the percentage evaluated using 500  $\mu\text{m}$  setup considering the standard deviations. Contrastingly, only  $6.3 \pm 0.1\%$  of Mg<sup>2+</sup> was deposited on graphite cathode. In addition, the evolution of Ca<sup>2+</sup> concentration is depicted in Fig. 6(b). Reproducible trends of Ca<sup>2+</sup>

deposition, relatively to the aforementioned  $\text{Mg}^{2+}$  deposition, were observed for the reactor configurations involving both 500  $\mu\text{m}$  and 3000  $\mu\text{m}$  interelectrode gaps. More  $\text{Ca}^{2+}$  precipitation occurred under the configuration of 500  $\mu\text{m}$  compared to that of 3000  $\mu\text{m}$ . Under the 500  $\mu\text{m}$  configuration,  $\text{Ca}^{2+}$  deposited by  $43.2 \pm 5.6\%$  on stainless steel, whereas it precipitated slightly more on graphite cathode (i.e., by  $46.7 \pm 1.2\%$ ). In comparison with the 3000  $\mu\text{m}$   $d_{\text{elec}}$ ,  $\text{Ca}^{2+}$  precipitated by  $36.2 \pm 1.6\%$  on stainless steel versus  $40.0 \pm 3.3\%$  on graphite. Surprisingly, when 100  $\mu\text{m}$   $d_{\text{elec}}$  was used, a conflicting behavior was noticed again. It corresponded to the configuration in which  $\text{CaCO}_3$  electro-precipitation occurred the most at the stainless steel cathode ( $55.1 \pm 2.2\%$ ), compared with the graphite electrode ( $9.0 \pm 1.2\%$ ). The evolution of TIC concentrations illustrated in **Fig. 6(c)** followed similar deduction drawn for the fate of  $\text{Ca}^{2+}$ . TIC decreased the most at  $d_{\text{elec}} = 100 \mu\text{m}$  with stainless steel as cathode. Comparatively, more carbonate deposition occurred under  $d_{\text{elec}} = 500 \mu\text{m}$  setup as compared to  $d_{\text{elec}} = 3000 \mu\text{m}$ , with marginally more electro-precipitation evaluated on graphite cathode in comparison to stainless steel for both  $d_{\text{elec}}$ .

To summarize, more electro-precipitation was formed under the 500  $\mu\text{m}$  configuration (microfluidic) in comparison to that of 3000  $\mu\text{m}$  (millimetric) and slightly more electro-precipitation took place on graphite cathode relatively to the stainless steel. The worst electro-precipitation occurred using 100  $\mu\text{m}$  (microfluidic)  $d_{\text{elec}}$  but only when stainless steel was used as cathode. Contrastingly, the slowest electro-precipitation was found also using the 100  $\mu\text{m}$   $d_{\text{elec}}$  but with graphite on cathode. Upon these results, two general conclusions could be assumed: (1) interelectrode distance played a determining role towards the formation of electro-precipitation and (2) under very particular operating conditions (i.e., submillimetric  $d_{\text{elec}}$  equals or lower than 100  $\mu\text{m}$ ), graphite properties could help to reduce the kinetics of deposition unlike any other experimental conditions.

To further understand this disparity of electro-precipitation in function of cathode material as well as  $d_{\text{elec}}$ , the polarization curves in cathodic region on stainless steel and graphite at 100, 500 and 3000  $\mu\text{m}$  gaps were performed (**Fig. 7**). According to **Fig. 7(a)**, it was observed that the HEP was lower

using a graphite cathode in comparison to stainless steel at 500  $\mu\text{m}$   $d_{\text{elec}}$ . As a result, when 200 mA current was applied (i.e., 4 mA  $\text{cm}^{-2}$ ), approximately -1.54 V/Ag-AgCl was measured on stainless steel, whilst -1.72 V/Ag-AgCl was recorded on graphite. Similarly, according to **Fig. 7(b)**, when the cell was used with 3000  $\mu\text{m}$   $d_{\text{elec}}$ , the HEP was also lower at 200 mA on graphite (-1.97 V/Ag-AgCl) than on the stainless steel (-1.91 V/Ag-AgCl) cathodes. Significantly lower applied  $E_C$  (into the water reduction region) measured under the macrometric reactor setup (3000  $\mu\text{m}$ ) could explain the lesser degree of electro-precipitation under this configuration. Intense competitive  $\text{H}_2$  evolution on cathode surface reduced the reactive site for precipitating reactions and in the same time induced partial deposit detachment from the cathode surface. This observation follows the deduction made in a previous study [36], where the role of  $d_{\text{elec}}$  was thoroughly discussed and modeled. The difference in electro-precipitation formation on both cathode materials at a given  $d_{\text{elec}}$  reciprocates the deduction drawn in **Section 3.1.2**. Higher porosity on graphite led to slightly higher local alkalization on graphite. As a consequence, there was a marginally higher driving force of thermodynamic shift of **Eqs. (6)-(8)** to the right, in the direction of mineral scaling production.



This conclusion was supported by higher  $S_{\text{elec}}$  for electronic transfers (85 vs. 80  $\text{cm}^2$  of stainless steel (**Section 3.1.1**)), which led to better electrochemical and/or chemical reactions. On the contrary, a reversal trend was noticed in the case where the microfluidic cell was used with  $d_{\text{elec}} = 100 \mu\text{m}$ . In accordance with **Fig. 7(c)**, it was observed that the HEP was higher on graphite rather than on stainless steel cathode. Consequently, the  $E_C$  was measured at -1.33 V/Ag-AgCl on graphite against -1.45 V/Ag-AgCl on stainless steel when 200 mA was applied. Visually, no gas bubble was produced under this configuration. Thus, the little precipitation observed was not induced by scaling detachment. At this higher measured  $E_C$ , less  $\text{OH}^-$  ions were produced on graphite, which lowered the kinetics of

Mg(OH)<sub>2</sub> and CaCO<sub>3</sub> deposition. Therefore, this finding might explain the contrasting observation made between the two cathode materials when 100 μm  $d_{\text{elec}}$  was adopted. This was the only condition where the carbonaceous graphite would substantially minimize the formation of mineral scaling.

The difference in the occurrence of mineral scaling on graphite and stainless steel inside microfluidic and millimetric reactors could be further emphasized by the evolution of bulk pH during the electrolysis (**Fig. 6(d)**). The decreasing pH value correlated with the OH<sup>-</sup> ion consumption shown in **Eqs. (6)** and **(7)** to form mineral precipitates. The more pH decreased, the more electro-precipitate formed on cathode surface, which was in agreement with the curves depicted in **Figs. 6(b)** and **6(c)**. Only bulk pH corresponding to the microfluidic setup (100 μm) using graphite cathode increased over time. It corroborated with the fact that this was the only configuration where sluggish mineral scaling was spotted (**Fig. 6**). The pH evolution depicted in **Fig. 6(d)** again confirmed the accumulation of OH<sup>-</sup> near porous cathode when graphite was used, which resulted in an increasing H<sup>+</sup> accumulation in the bulk **[48]**. Thus, the pH dropped.

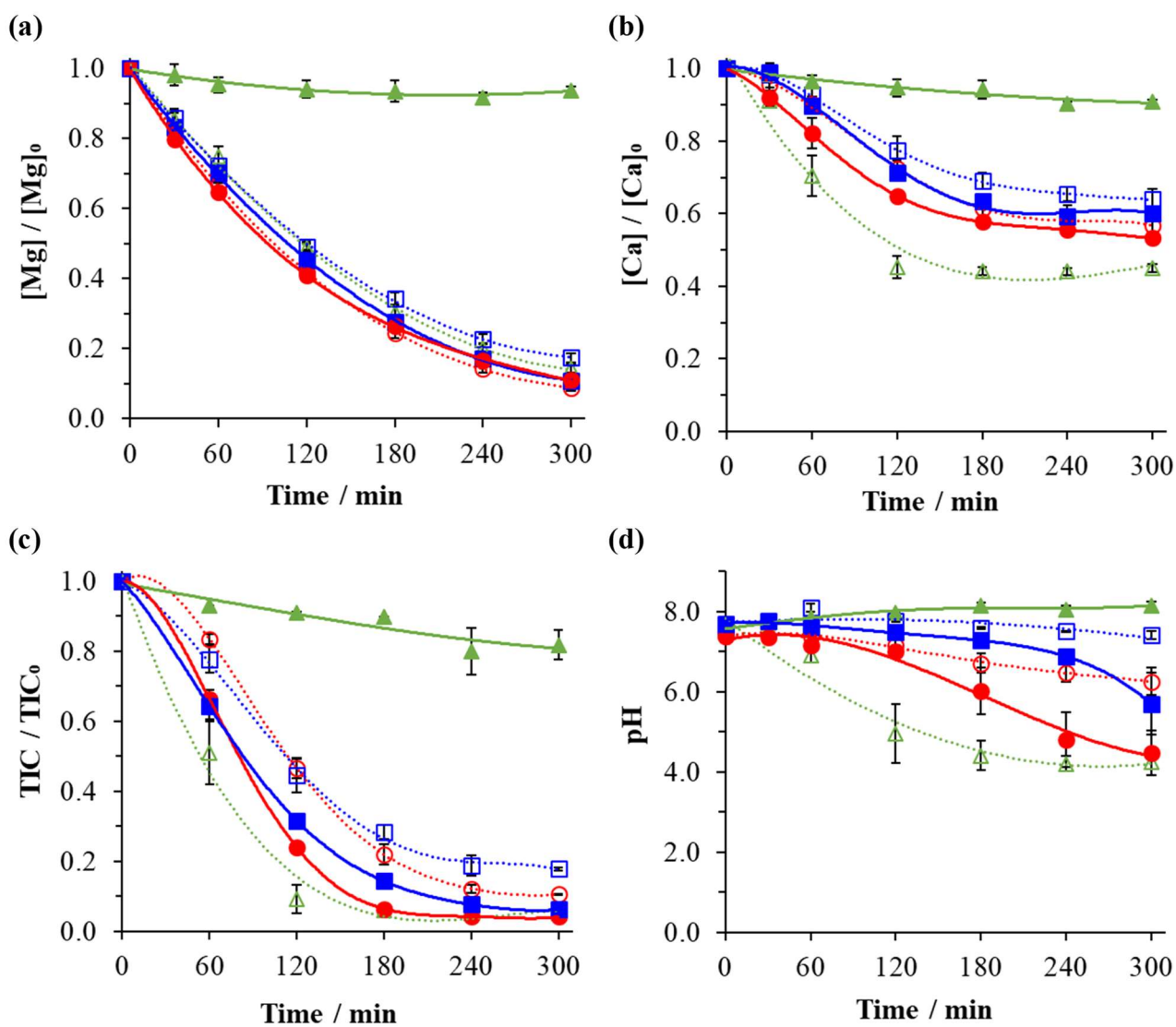


**Fig. 6.** Concentrations of (a)  $Mg^{2+}$ , (b)  $Ca^{2+}$ , (c) TIC and (d) bulk pH during the electrolysis of solution initially containing  $150 \text{ mg L}^{-1} Ca^{2+}$ ,  $5 \text{ mg L}^{-1} Mg^{2+}$  and  $60 \text{ mg-C L}^{-1}$  of TIC at 200 mA.

$d_{elec}$  of ( $\triangle$ ,  $\blacktriangle$ ): 100, ( $\circ$ ,  $\bullet$ ): 500 and ( $\square$ ,  $\blacksquare$ ): 3000  $\mu\text{m}$  were evaluated using ( $\blacktriangle$ ,  $\bullet$ ,  $\blacksquare$ ): graphite and ( $\triangle$ ,  $\circ$ ,  $\square$ ): stainless steel cathode. Anode: BDD.

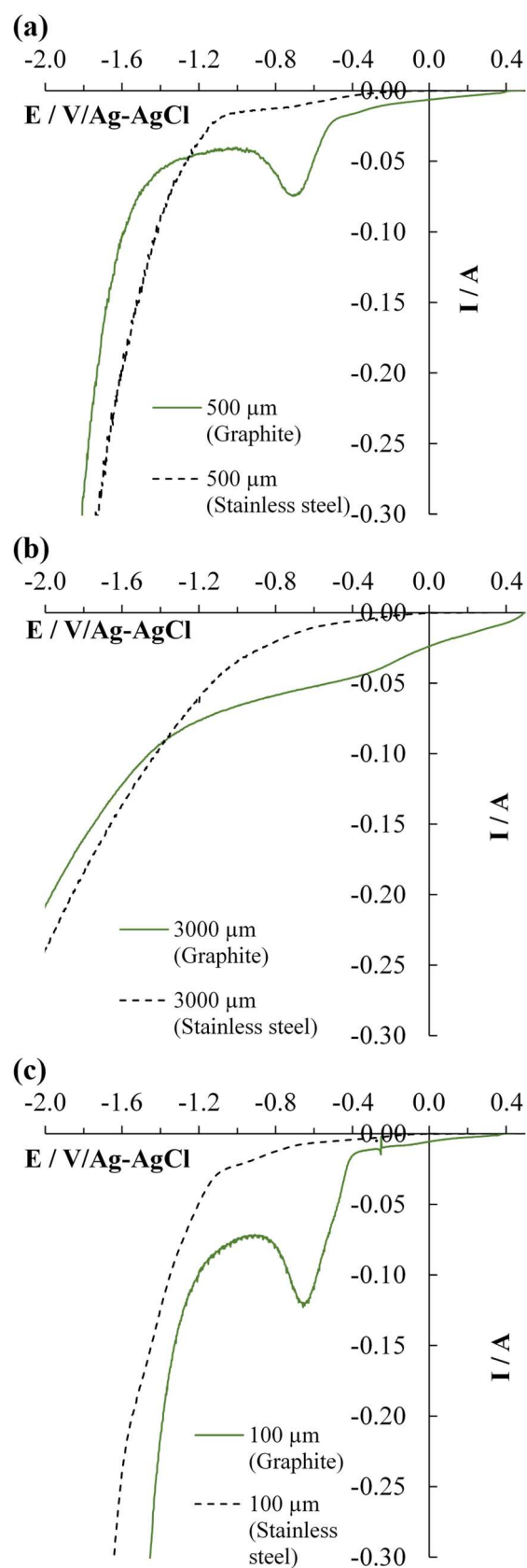


**Fig. 7.** LSV of stainless steel and graphite plate cathodes when they were mounted in an electrochemical cell with  $d_{\text{elec}} =$  **(a)** 500, **(b)** 3000 and **(c)** 100  $\mu\text{m}$ . The potential was swept between 0.5 to -1.8 V/Ag-AgCl with a scan rate of  $10 \text{ mV s}^{-1}$ . CE: BDD, REF: Ag-AgCl.

### 3.2.2. Cathode/electrolyte interface study of electro-precipitation on graphite and stainless steel by electrochemical impedance technique

EIS analysis was performed on graphite and compared to stainless steel in order to characterize mineral electro-precipitation during the electrolysis at 100, 500 and 3000  $\mu\text{m}$  interelectrode gaps. The evolutions of  $R_{\text{CT}}$  and  $C_{\text{DL}}$  using graphite cathode are plotted in **Fig. 8**. It can be noticed that the values of  $R_{\text{CT}}$  appeared constant during the electrolysis for all three  $d_{\text{elec}}$  (**Figs. 8(a), 8(c) and 8(e)**).  $R_{\text{CT}}$  measured on graphite took the average values of  $0.42 \pm 0.10$ ,  $0.88 \pm 0.05$  and  $2.96 \pm 0.10 \Omega$  respectively, when 100, 500 and 3000  $\mu\text{m}$   $d_{\text{elec}}$  were used. Despite the formation of electro-precipitation in the configurations of 500 and 3000  $\mu\text{m}$ , the graphite surface was also not fully passivated. This was in-trend with the conclusion obtained in a previous study [36], using stainless steel as cathode. As for the evolution of  $C_{\text{DL}}$  illustrated in **Figs. 8(b), 8(d) and 8(f)**, it was noticed that they rather increased during the electrolysis unlike the evolution of  $C_{\text{DL}}$  on stainless steel cathode. It increased by 58, 76 and 37% in the respective order of 100, 500 and 3000  $\mu\text{m}$  reactor configurations. This increase of  $C_{\text{DL}}$  values had no significant relation with the formation of electro-precipitate since it also increased when 100  $\mu\text{m}$   $d_{\text{elec}}$  was used (a condition where the least mineral scaling took place). Instead, it has something to do with the porosity of graphite and will be discussed shortly when it is compared to stainless steel cathode. With respect to the evolution of film resistance ( $R_{\text{F}}$ ) formed on graphite during the electrolysis plotted in **Fig. 9**, it was observed that  $R_{\text{F}}$  increased during the first 2 h of electrolysis to  $0.29 \pm 0.01$  and  $0.43 \pm 0.15 \Omega$  for 500 and 3000  $\mu\text{m}$  setup, respectively. It was expected to measure higher  $R_{\text{F}}$  value using 500  $\mu\text{m}$   $d_{\text{elec}}$  since marginally more scaling occurred at this distance, but the opposite trend was obtained. Nonetheless, after 2 h electrolysis, reproducible trend was noticed on both interelectrode gaps in line with the kinetics of precipitation previously discussed in **Section 3.1.2** and **Section 3.2.1**.  $R_{\text{F}}$  values in both conditions decreased and it could be ascribed to the evolution of bulk pH in reference to **Fig. 6(d)**. The fact that the electro-precipitate had the possibility to re-dissolve into the solution apparently decreased the resistance related to the

precipitated film. This might be the reason why  $R_F$  values decreased using both  $d_{\text{elec}}$  after 2 h of electrolysis as depicted in **Fig. 9**.

Upon comparing the interfacial activities between graphite and stainless steel, some differences could be highlighted. The ratio of  $R_{\text{CT}}$  and  $C_{\text{DL}}$  values between graphite and stainless steel for all investigated  $d_{\text{elec}}$  configurations are illustrated in **Fig. 8**. It can be observed that  $R_{\text{CT}}$  values on graphite were lower than those on stainless steel, i.e., averagely by 0.6-fold, 0.8-fold and 0.7-fold using 100, 500 and 3000  $\mu\text{m}$ , respectively in all conditions. This lower  $R_{\text{CT}}$  value characterized by EIS on graphite versus stainless steel corroborates the corresponding  $R_{\text{CT}}$  values determined using  $I_0$  method in **Section 3.1.1**. Lower  $R_{\text{CT}}$  measured on graphite correlates with the finding that more electro-precipitation took place on porous graphite (except 100  $\mu\text{m}$ ). Easier electronic exchanges would favor a higher  $\text{OH}^-$  production and subsequently a better precipitation reaction of  $\text{CaCO}_3$  and  $\text{Mg}(\text{OH})_2$ . On the contrary,  $C_{\text{DL}}$  values were higher on graphite in comparison to the values measured on stainless steel by an average factor of 2.7, 1.1 and 1.5 using 100, 500 and 3000  $\mu\text{m}$ , respectively. These differences were accounted for the porous properties of graphite. Higher  $S_{\text{elec}}$  offered by porous cathode would allow higher distribution of electronic double layer. This finding was in agreement with the results documented by Da Silva et al. [71]. They found that  $C_{\text{DL}}$  value measured on porous metal oxide electrode was significantly reduced when the porosity of the electrode was decreased.

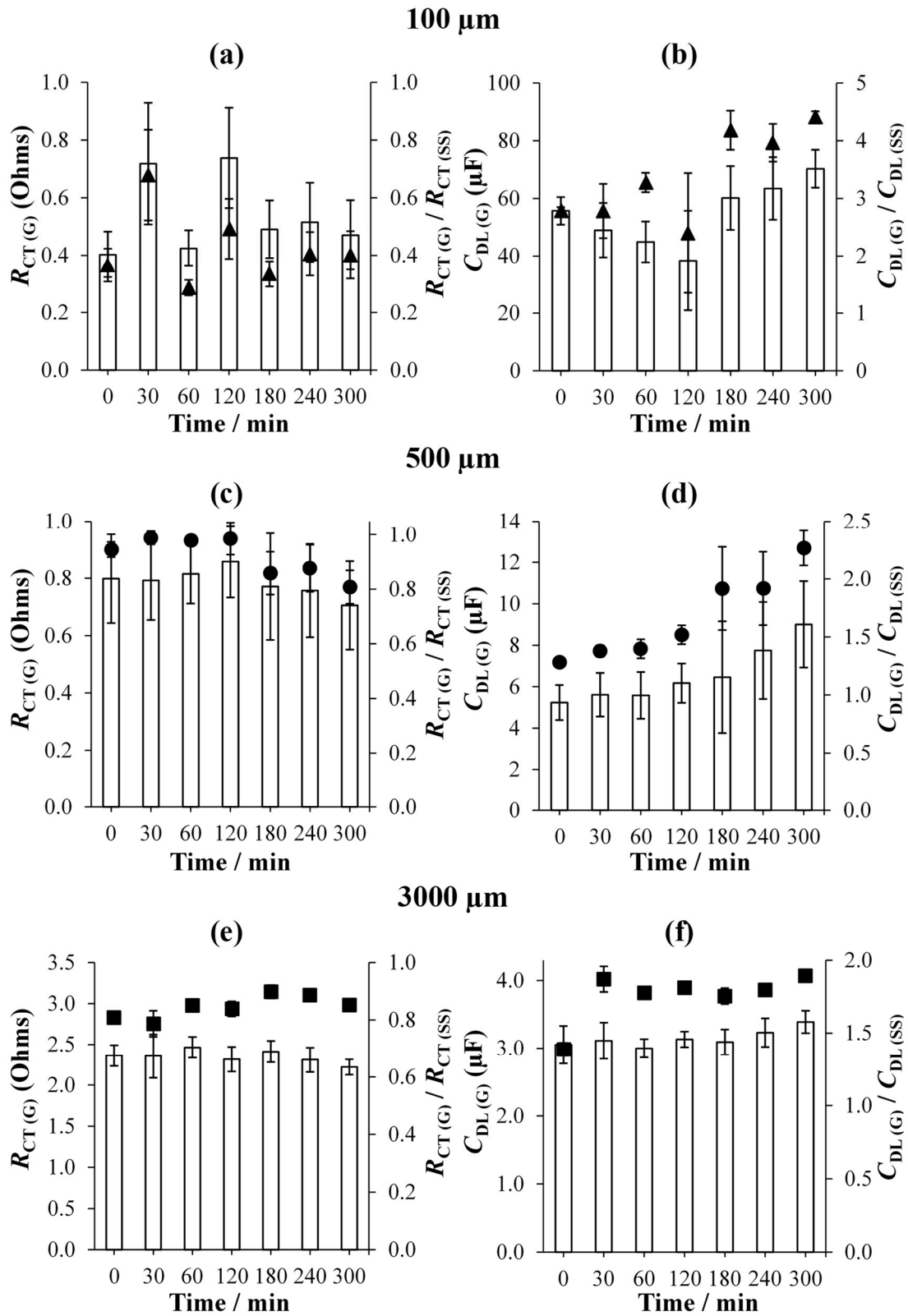


**Fig. 8.** Evolutions of  $R_{CT(G)}$  ( $\blacktriangle$ ,  $\bullet$ ,  $\blacksquare$ ) and  $R_{CT(G)}/R_{CT(SS)}$  ( $\square$ ) ((a), (c), (e)) as well as  $C_{DL(G)}$  ( $\blacktriangle$ ,  $\bullet$ ,  $\blacksquare$ ) and  $C_{DL(G)}/C_{DL(SS)}$  ( $\square$ ) ((b), (d), (f)) during the electrolysis of solution containing  $\text{Ca}^{2+}$  150  $\text{mg L}^{-1}$ ,  $\text{Mg}^{2+}$  5  $\text{mg L}^{-1}$  and TIC 60  $\text{mg L}^{-1}$ . ( $\blacktriangle$ ): 100  $\mu\text{m}$  ((a), (b)), ( $\bullet$ ): 500  $\mu\text{m}$  ((c), (d)) and ( $\blacksquare$ ): 3000  $\mu\text{m}$  ((e), (f)).

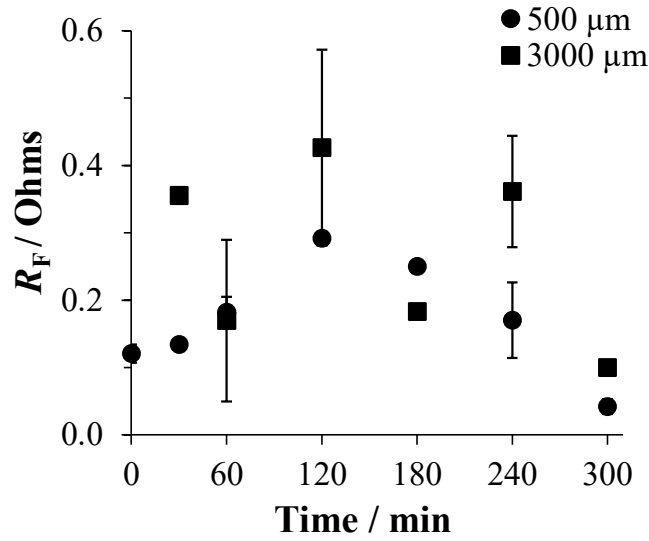


**Fig. 9.** Evolutions of  $R_F$  during the electrolysis of solution initially containing  $\text{Ca}^{2+}$   $150 \text{ mg L}^{-1}$ ,  $\text{Mg}^{2+}$   $5 \text{ mg L}^{-1}$  and TIC  $60 \text{ mg L}^{-1}$ . (●):  $500 \mu\text{m}$  and (■):  $3000 \mu\text{m}$ .

### 3.2.3. Interdependence of cathode potential, $\text{H}_2$ evolution overpotential and cathode porosity on electro-precipitation

Previous results in [Section 3.1](#) and [Section 3.2](#) emphasized interdependence of  $E_C$  with HEP, cathode porosity and hydrophobicity on the evolution of electro-precipitation. [Figure 10](#) displays a flow chart summarizing the influence of  $E_C$  and therefore of  $d_{\text{elec}}$  and the current density, on the kinetics of  $\text{CaCO}_3$  electro-precipitation depending on the porosity and hydrophobicity of the cathode material. It emphasizes the fact that higher  $d_{\text{elec}}$  led to lower electro-precipitation with low porosity material and inversely. It is additionally proposed to introduce a new empirical criterion (i.e.,  $E_C/\text{HEP}$ ) that consider both operating condition ( $d_{\text{elec}}$ ) and cathode material property (HEP).  $E_C$  depends on the cell voltage, which also depends on  $d_{\text{elec}}$  [\[36\]](#). Moreover, by assimilating the overpotential to HEP, then  $E_C$  is equal to the sum of HEP and the cathode potential at equilibrium ( $E_{0C}$ ), which highlights the direct link between  $E_C$  and HEP.

**Table 1** regroups the values of HEP, the ratio between  $E_C$  over HEP and the percentage of  $\text{CaCO}_3$  precipitation as a function of  $d_{\text{elec}}$  at 200 mA for stainless steel and graphite cathodes. The ratio of  $E_C/\text{HEP}$  for different cathode porosities and  $d_{\text{elec}}$  were then calculated with regard to the resulting  $\text{CaCO}_3$  electro-precipitation and they are illustrated in **Fig. 11**. Only  $\text{CaCO}_3$  was chosen because (1) it represents the predominant mineral scaling occurring under the applied operating conditions and (2) to simplify the plot of the inter-relation mechanistic scheme. For the values of  $E_C/\text{HEP}$  inferior to  $\sim 1.3$  for porous graphite and stainless steel, the percentage of  $\text{CaCO}_3$  precipitation increased against  $E_C/\text{HEP}$  (**Fig. 11**). Interestingly, the ratio of 1.3 represented the maximal point for mineral scaling formation for graphite and stainless steel respectively. As the ratio  $E_C/\text{HEP}$  was displaced beyond these points, the percentage of  $\text{CaCO}_3$  deposition decreased as a result of antagonism effect of  $\text{H}_2$  gas evolution that promoted detachment of precipitates. In the aim to compare with  $E_C/\text{HEP}$  ratio obtained from a previous study dealing on electro-precipitation, a  $E_C/\text{HEP}$  ratio of 0.02 at  $d_{\text{elec}} = 50 \mu\text{m}$  leading to the absence of electro-precipitation with stainless steel cathode was found [36]. This point has been added to **Fig. 11** and seems to be consistent with the trend obtained with the present data.

It is further important to note that this interdependence behavior at cathode surface could interfere the EAOPs efficiency in presence of real matrices that particularly contains  $\text{Mg}^{2+}$  and/or  $\text{Ca}^{2+}$  and  $\text{HCO}_3^-/\text{CO}_3^{2-}$ . For example, porous carbon materials are preferentially used for electro-Fenton system for their ability to electrogenerate more  $\text{H}_2\text{O}_2$  and to promote the subsequent Fenton reaction. Only few previous studies investigated the influence of water hardness on electro-Fenton efficiency [72, 73]. They attributed the decrease of organic pollutant removal to the formation of complexes with calcium and magnesium in the bulk. However, they did not consider the cathodic electro-precipitation phenomenon that should preferentially occur and could progressively passivate the cathode. Moreover, the present criterion could be used in EAOPs optimization in order to limit the electro-precipitation issues.

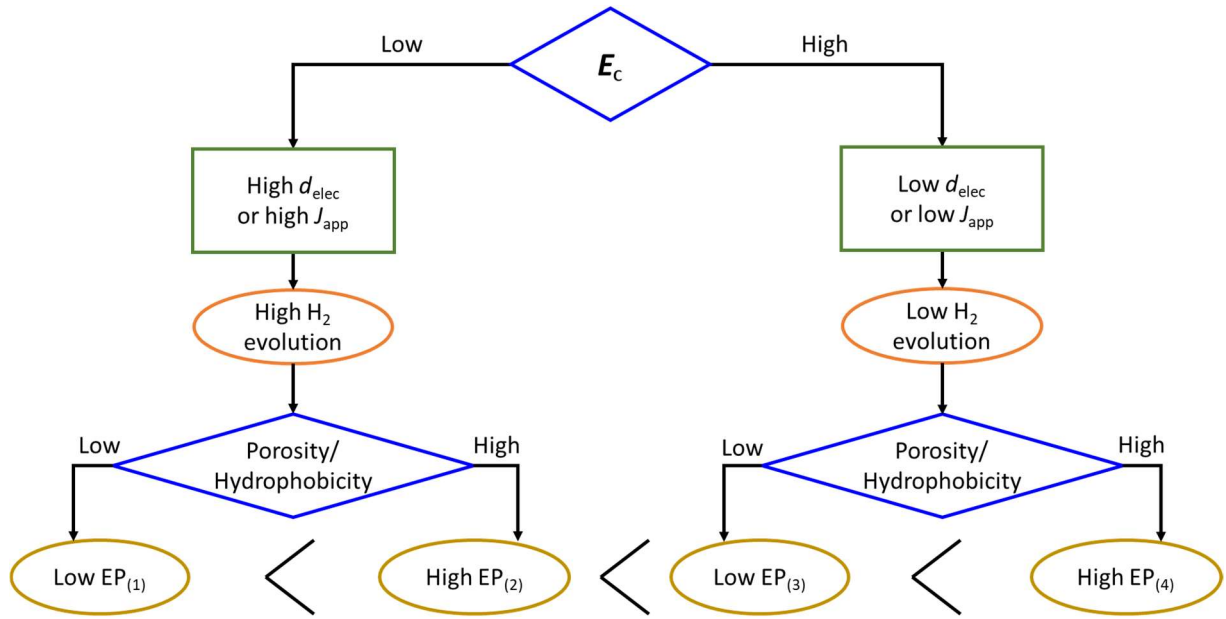


**Fig. 10.** Flow chart taking into account  $E_c$ ,  $d_{elec}$ , current density,  $H_2$  gas evolution, porosity/hydrophobicity on global  $CaCO_3$  electro-precipitation (EP) efficiency, with the following general order of electro-precipitation yield (from the lowest to the highest):  $EP_{(1)} < EP_{(2)} < EP_{(3)} < EP_{(4)}$ .

**Table 1.** Values of HEP, ratio of  $E_c$ /HEP and percentage of  $CaCO_3$  electro-precipitation (after 5 h of electrolysis) as a function of  $d_{elec}$  under the polarization of 200 mA for stainless steel and graphite cathode.

$d_{elec}$ ( $\mu m$ )	Stainless steel			Graphite		
	HEP (V/Ag-AgCl)	$E_c$ /HEP	% Precip.	HEP (V/Ag-AgCl)	$E_c$ /HEP	% Precip.
100	-1.1	1.32	$55.1 \pm 2.2$	-1.1	1.21	$9.0 \pm 1.2$
500	-1.1	1.40	$43.2 \pm 5.6$	-1.3	1.32	$46.7 \pm 1.2$
3000	-0.9	2.12	$36.2 \pm 1.6$	-1.0	1.97	$40.0 \pm 3.3$

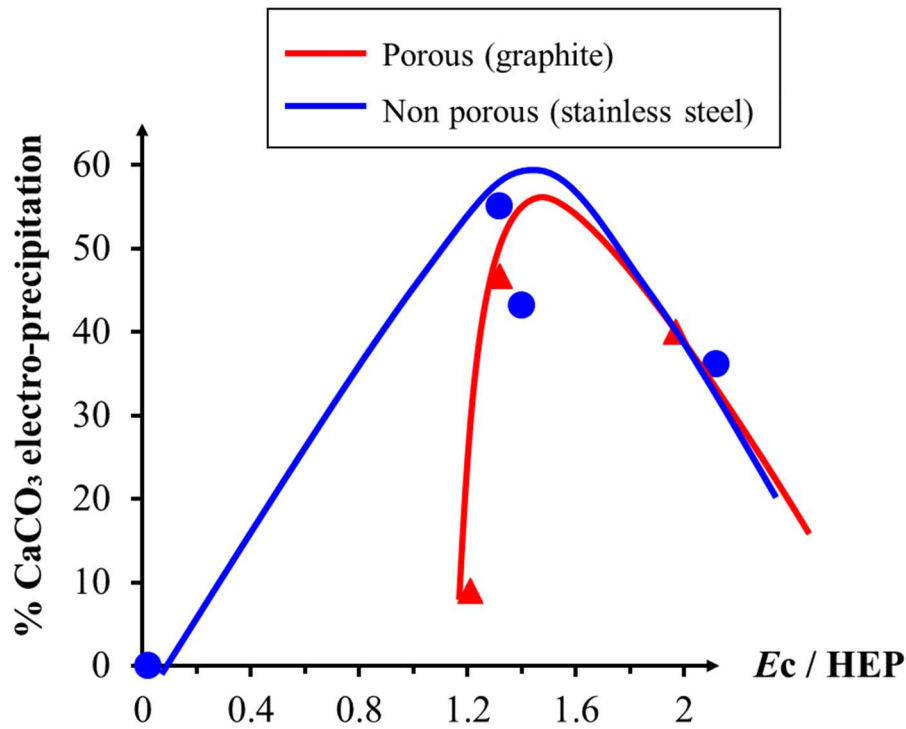


**Fig. 11.** Mechanistic scheme giving general trends of inter-relation between  $E_c$ , HEP and porosity towards  $\text{CaCO}_3$  electro-precipitation on graphite and stainless steel cathodes.

#### 4. Conclusions

The role of cathode materials on cathodic electro-precipitation was newly investigated in this article and particularly under submillimetric configuration compared with more conventional millimetric interelectrode gaps. Non-porous and non-carbonaceous stainless steel as well as carbonaceous graphite plate and carbon paper which possessed different porosities were compared. Electroactive surface area of stainless steel, graphite and carbon paper were determined via electrochemical method. Values of 80, 85 and 175  $\text{cm}^2$  were obtained for stainless steel, graphite and carbon paper, respectively. It indicated that different cathode materials offered different number of sites for electronic exchanges on top of having different porosities. The main new insights given by this study are summarized as follows:

- $\text{Mg}(\text{OH})_2$  precipitated little on stainless steel, graphite and carbon paper at low applied current (20 mA), whilst  $\text{CaCO}_3$  electro-precipitation was formed only on stainless steel and graphite cathode but not on carbon paper.
- Using higher applied current (200 mA), a significant precipitation of  $\text{Mg}(\text{OH})_2$  was observed on stainless steel and graphite, but a low precipitation on carbon paper. However, quick  $\text{CaCO}_3$  deposition was noted on carbon paper. Meanwhile, slightly favored  $\text{CaCO}_3$  electro-precipitation on graphite in comparison to stainless steel was observed and it was ascribed to higher local pH due to porous characteristic of graphite.
- Lower HEP would only lead to more formation of electro-precipitates. It was due to enhanced  $\text{OH}^-$  production that would consequently favor the mineral scaling. Slightly less mineral scaling could be achieved if the HER overpotential was very low into the water reduction region (where the competing  $\text{H}_2$  evolution rigorously evolved on cathode surface).
- The role of HEP was overshadowed by an additional rate limiting parameter, i.e.,  $E_C$  that need to be also considered. When stainless steel was used as cathode under the  $100 \mu\text{m } d_{\text{elec}}$  setup, the most electro-precipitation took place. Contrastingly, by replacing stainless steel with graphite, the slowest mineral scaling was noticed. It was due to the alteration in the cathode potential value where the  $\text{OH}^-$  production was less favorable.
- The introduction of a new criterion, i.e.,  $E_C/\text{HEP}$  ratio, permit to consider the interdependency of operating conditions ( $d_{\text{elec}}$ ) with the cathode material characteristics. A maximal  $\text{CaCO}_3$  electro-precipitation was noticed at an optimal  $E_C/\text{HEP}$  ratio  $\sim 1.3$  porous and nonporous cathodes. This should help to predict the range of  $E_C$  to apply for either maximal or minimal scaling at a given cathode material.
- Using electrochemical impedance analysis, the porosity of graphite was evidenced. Higher  $C_{\text{DL}}$  was determined on graphite compared to stainless steel. Lower  $R_{\text{CT}}$  measured on graphite proved that better electronic transfers take place on graphite in comparison with stainless steel cathode.

In overall, due to rapid  $\text{CaCO}_3$  deposition as well as acidic post-treatment condition, porous carbon paper was not a suitable cathode to be chosen if the minimization of electro-precipitation is sought. Nonetheless, it has been proven herein that slow kinetic growth of deposit could however be devised using graphite or other materials under the condition where the applied cathode potential does not favor the  $\text{OH}^-$  production. Meanwhile, carbonaceous materials would suit the purpose of the recovery of waste containing added-value compound via an electrochemical precipitation technique. They are relatively cheaper than other materials hence offering an economical advantage for the electrochemical process to be implemented. Finally, the electro-precipitation phenomena should be considered in EAOPs with real matrices and the new criterion developed could be used to improve the optimization.

## **Acknowledgements**

Authors would like to thank French Ministry of Higher Education, Research and Innovation (MESRI) for financial support of Faidzul Hakim Adnan's doctorate program, as well as other grants provided by Carnot ICEEL, LTSER Zone Atelier du Bassin de la Moselle (ZAM) and European regional development fund program (CPER SusChemProc).

## References

- [1] P. Simon, Y. Gogotsi, Materials for electrochemical capacitors, *Nature Materials*, 7 (2008) 845-854.
- [2] R.L. McCreery, Advanced carbon electrode materials for molecular electrochemistry, *Chemical Reviews*, 108 (2008) 2646-2687.
- [3] C. Hu, L. Dai, Carbon-based metal-free catalysts for electrocatalysis beyond the ORR, *Angewandte Chemie International Edition*, 55 (2016) 11736-11758.
- [4] F. Yin, W. Yue, Y. Li, S. Gao, C. Zhang, H. Kan, H. Niu, W. Wang, Y. Guo, Carbon-based nanomaterials for the detection of volatile organic compounds: A review, *Carbon*, 180 (2021) 274-297.
- [5] F.C. Moreira, R.A.R. Boaventura, E. Brillas, V.J.P. Vilar, Electrochemical advanced oxidation processes: A review on their application to synthetic and real wastewaters, *Applied Catalysis B: Environmental*, 202 (2017) 217-261.
- [6] O. Garcia-Rodriguez, E. Mousset, H. Olvera-Vargas, O. Lefebvre, Electrochemical treatment of highly concentrated wastewater: A review of experimental and modeling approaches from lab- to full-scale, *Critical Reviews in Environmental Science and Technology*, 52 (2020) 240-309.
- [7] E. Mousset, Z. Wang, J. Hammaker, O. Lefebvre, Electrocatalytic phenol degradation by a novel nanostructured carbon fiber brush cathode coated with graphene ink, *Electrochimica Acta*, 258 (2017) 607-617.
- [8] A. Kulkarni, S. Siahrostami, A. Patel, J.K. Nørskov, Understanding catalytic activity trends in the oxygen reduction reaction, *Chemical Reviews*, 118 (2018) 2302-2312.
- [9] X. Du, M.A. Oturan, M. Zhou, N. Belkessa, P. Su, J. Cai, C. Trelu, E. Mousset, Nanostructured electrodes for electrocatalytic advanced oxidation processes: From materials preparation to mechanisms understanding and wastewater treatment applications, *Applied Catalysis B: Environmental*, 296 (2021) 120332.
- [10] W. Wang, X. Lu, P. Su, Y. Li, J. Cai, Q. Zhang, M. Zhou, O. Arotiba, Enhancement of hydrogen peroxide production by electrochemical reduction of oxygen on carbon nanotubes modified with fluorine, *Chemosphere*, 259 (2020) 127423.
- [11] M.A. Oturan, J.-J. Aaron, Advanced oxidation processes in water/wastewater treatment: Principles and applications. A review, *Critical Reviews in Environmental Science and Technology*, 44 (2014) 2577-2641.
- [12] M.A. Oturan, Outstanding performances of the BDD film anode in electro-Fenton process: Applications and comparative performance, *Current Opinion in Solid State and Materials Science*, 25 (2021) 100925.
- [13] C.A. Martínez-Huitle, M. Panizza, Electrochemical oxidation of organic pollutants for wastewater treatment, *Current Opinion in Electrochemistry*, 11 (2018) 62-71.
- [14] E. Mousset, C. Trelu, H. Olvera-Vargas, Y. Pechaud, F. Fourcade, M.A. Oturan, Electrochemical technologies coupled with biological treatments, *Current Opinion in Electrochemistry*, 26 (2021) 100668.

- [15] E. Mousset, W.H. Loh, W.S. Lim, L. Jarry, Z. Wang, O. Lefebvre, Cost comparison of advanced oxidation processes for wastewater treatment using accumulated oxygen-equivalent criteria, *Water Research*, 200 (2021) 117234.
- [16] I. Sirés, E. Brillas, M.A. Oturan, M.A. Rodrigo, M. Panizza, Electrochemical advanced oxidation processes: Today and tomorrow. A review, *Environmental Science and Pollution Research*, 21 (2014) 8336-8367.
- [17] C.A. Martínez-Huitle, M.A. Rodrigo, I. Sirés, O. Scialdone, Single and coupled electrochemical processes and reactors for the abatement of organic water pollutants: A critical review, *Chemical Reviews*, 115 (2015) 13362-13407.
- [18] A.A.G.D. Amarasooriya, T. Kawakami, Removal of co-existing fluoride, calcium, magnesium, and carbonates, by non-chemical induced electrolysis system for drinking and industrial purposes, *H2Open Journal*, 3 (2020) 10-31.
- [19] C. Gabrielli, G. Maurin, H. Francy-Chausson, P. Thery, T.T.M. Tran, M. Tlili, Electrochemical water softening: principle and application, *Desalination*, 201 (2006) 150-163.
- [20] Y. Lei, J.C. Remmers, M. Saakes, R.D. van der Weijden, C.J.N. Buisman, Is there a precipitation sequence in municipal wastewater induced by electrolysis?, *Environmental Science & Technology*, 52 (2018) 8399-8407.
- [21] Y. Lei, I. Hidayat, M. Saakes, R. van der Weijden, C.J.N. Buisman, Fate of calcium, magnesium and inorganic carbon in electrochemical phosphorus recovery from domestic wastewater, *Chemical Engineering Journal*, 362 (2019) 453-459.
- [22] Y. Lei, Z. Zhan, M. Saakes, R.D. van der Weijden, C.J.N. Buisman, Electrochemical recovery of phosphorus from wastewater using tubular stainless-steel cathode for a scalable long-term operation, *Water Research*, 199 (2021) 117199.
- [23] Y. Takabe, M. Fujiyama, Y. Yamasaki, T. Masuda, Influences of electrode distance and electrolysis time on phosphorus precipitation and composition during electrolysis of anaerobic digestion effluent, *Science of The Total Environment*, 803 (2022) 150114.
- [24] K.-H. Yeon, J.-H. Song, J. Shim, S.-H. Moon, Y.-U. Jeong, H.-Y. Joo, Integrating electrochemical processes with electro-dialysis reversal and electro-oxidation to minimize COD and T-N at wastewater treatment facilities of power plants, *Desalination*, 202 (2007) 400-410.
- [25] C. Deslouis, I. Frateur, G. Maurin, B. Tribollet, Interfacial pH measurement during the reduction of dissolved oxygen in a submerged impinging jet cell, *Journal of Applied Electrochemistry*, 27 (1997) 482-492.
- [26] M.M. Tlili, M. Benamor, C. Gabrielli, H. Perrot, B. Tribollet, Influence of the interfacial pH on electrochemical CaCO<sub>3</sub> precipitation, *Journal of The Electrochemical Society*, 150 (2003) C765.
- [27] F.H. Adnan, E. Mousset, S. Pontvianne, M.-N. Pons, Mineral cathodic electro-precipitation and its kinetic modelling in thin-film microfluidic reactor during advanced electro-oxidation process, *Electrochimica Acta*, 387 (2021).
- [28] O. Scialdone, E. Corrado, A. Galia, I. Sirés, Electrochemical processes in macro and microfluidic cells for the abatement of chloroacetic acid from water, *Electrochimica Acta*, 132 (2014) 15-24.

- [29] P. Ma, H. Ma, S. Sabatino, A. Galia, O. Scialdone, Electrochemical treatment of real wastewater. Part 1: Effluents with low conductivity, *Chemical Engineering Journal*, 336 (2018) 133-140.
- [30] J.F. Pérez, J. Llanos, C. Sáez, C. López, P. Cañizares, M.A. Rodrigo, Development of an innovative approach for low-impact wastewater treatment: A microfluidic flow-through electrochemical reactor, *Chemical Engineering Journal*, 351 (2018) 766-772.
- [31] J.F. Pérez, J. Llanos, C. Sáez, C. López, P. Cañizares, M.A. Rodrigo, Towards the scale up of a pressurized-jet microfluidic flow-through reactor for cost-effective electro-generation of H<sub>2</sub>O<sub>2</sub>, *Journal of Cleaner Production*, 211 (2019) 1259-1267.
- [32] F.H. Adnan, M.N. Pons, E. Mousset, Thin film microfluidic reactors in electrochemical advanced oxidation processes for wastewater treatment: A review on influencing parameters, scaling issues, and engineering considerations, *Electrochemical Science Advances*, n/a (2022) e2100210.
- [33] E. Mousset, Interest of micro-reactors for the implementation of advanced electrocatalytic oxidation with boron-doped diamond anode for wastewater treatment, *Current Opinion in Electrochemistry*, 32 (2022) 100897.
- [34] E. Mousset, Unprecedented reactive electro-mixing reactor: Towards synergy between micro- and macro-reactors?, *Electrochemistry Communications*, 118 (2020) 106787.
- [35] E. Mousset, M. Puce, M.N. Pons, Advanced electro-oxidation with boron-doped diamond for acetaminophen removal from real wastewater in a microfluidic reactor: Kinetics and mass-transfer studies, *ChemElectroChem*, 6 (2019) 2908-2916.
- [36] F.H. Adnan, S. Pontvianne, M.-N. Pons, E. Mousset, Unprecedented roles of submillimetric interelectrode distances and electrogenerated gas bubbles on mineral cathodic electro-precipitation: Modeling and interface studies, *Chemical Engineering Journal*, 431 (2022).
- [37] F.H. Adnan, M.-N. Pons, E. Mousset, Mass transport evolution in microfluidic thin film electrochemical reactors: New correlations from millimetric to submillimetric interelectrode distances, *Electrochemistry Communications*, 130 (2021).
- [38] T.X.H. Le, M. Bechelany, S. Lacour, N. Oturan, M.A. Oturan, M. Cretin, High removal efficiency of dye pollutants by electron-Fenton process using a graphene based cathode, *Carbon*, 94 (2015) 1003-1011.
- [39] E. Mousset, Z. Wang, J. Hammaker, O. Lefebvre, Physico-chemical properties of pristine graphene and its performance as electrode material for electro-Fenton treatment of wastewater, *Electrochimica Acta*, 214 (2016) 217-230.
- [40] A. Lissaneddine, M.-N. Pons, F. Aziz, N. Ouazzani, L. Mandi, E. Mousset, Electrosorption of phenolic compounds from olive mill wastewater: Mass transport consideration under a transient regime through an alginate-activated carbon fixed-bed electrode, *Journal of Hazardous Materials*, 430 (2022) 128480.
- [41] A.J. Bard, Faulkner, L.R., Double-layer structure and adsorption, in: J.W.S. Inc. (Ed.) *Electrochemical methods: Fundamentals and applications* 2001, pp. 534.
- [42] H. Saraç, M.A. Patrick, A.A. Wragg, Physical properties of the ternary electrolyte potassium ferri-ferrocyanide in aqueous sodium hydroxide solution in the range 10–90°C, *Journal of Applied Electrochemistry*, 23 (1993) 51-55.

- [43] A.A. Wragg, A.A. Leontaritis, Local mass transfer and current distribution in baffled and unbaffled parallel plate electrochemical reactors, *Chemical Engineering Journal*, 66 (1997) 1-10.
- [44] M. Griffiths, C.P. de León, F.C. Walsh, Mass transport in the rectangular channel of a filter-press electrolyzer (the FM01-LC reactor), *American Institute of Chemical Engineers*, 51 (2005) 682-687.
- [45] A.J. Bard, Faulkner, L.R., Kinetics of electrode reactions, in: J.W.S. Inc. (Ed.) *Electrochemical methods: Fundamentals and applications* 2001, pp. 87.
- [46] K. Oldham, J. Myland, A. Bond, *Electrode Polarization, Electrochemical science and technology: fundamentals and applications*, John Wiley & Sons 2011, pp. 193.
- [47] J.N. Butler, *Carbon dioxide equilibria and their applications*, 1st ed., Taylor & Francis Group, New York: Routledge, 1991.
- [48] Y. Lei, E. Geraets, M. Saakes, R.D. van der Weijden, C.J.N. Buisman, Electrochemical removal of phosphate in the presence of calcium at low current density: Precipitation or adsorption ? , *Water Research*, 169 (2020) 115207.
- [49] Y. Yu, H. Jin, X. Quan, B. Hong, X. Chen, Continuous multistage electrochemical precipitation reactor for water softening, *Industrial & Engineering Chemistry Research*, 58 (2019) 461-468.
- [50] I. Sanjuán, D. Benavente, V. García-García, E. Expósito, V. Montiel, Electrochemical softening of concentrates from an electrodialysis brackish water desalination plant: Efficiency enhancement using a three-dimensional cathode, *Separation and Purification Technology*, 208 (2019) 217-226.
- [51] Y. Fu, G. Lin, M. Hou, B. Wu, H. Li, L. Hao, Z. Shao, B. Yi, Optimized Cr-nitride film on 316L stainless steel as proton exchange membrane fuel cell bipolar plate, *International Journal of Hydrogen Energy*, 34 (2009) 453-458.
- [52] W. Song, H. Yu, Z. Shao, B. Yi, J. Lin, N. Liu, Effect of polytetrafluoroethylene distribution in the gas diffusion layer on water flooding in proton exchange membrane fuel cells, *Chinese Journal of Catalysis*, 35 (2014) 468-473.
- [53] H. Karoui, B. Riffault, M. Jeannin, A. Kahoul, O. Gil, M. Ben Amor, M.M. Tlili, Electrochemical scaling of stainless steel in artificial seawater: Role of experimental conditions on CaCO<sub>3</sub> and Mg(OH)<sub>2</sub> formation, *Desalination*, 311 (2013) 234-240.
- [54] C. Deslouis, D. Festy, O. Gil, V. Maillot, S. Touzain, B. Tribollet, Characterization of calcareous deposits in artificial sea water by impedances techniques: 2-deposit of Mg(OH)<sub>2</sub> without CaCO<sub>3</sub>, *Electrochimica Acta*, 45 (2000) 1837-1845.
- [55] S.M. Hoseinieh, T. Shahrabi, B. Ramezanzadeh, M.F. Rad, The role of porosity and surface morphology of calcium carbonate deposits on the corrosion behavior of unprotected API 5L X52 rotating disk electrodes in artificial seawater, *Journal of The Electrochemical Society*, 163 (2016) C515-C529.
- [56] D. Li, T. Zheng, Y. Liu, D. Hou, H. He, H. Song, J. Zhang, S. Tian, W. Zhang, L. Wang, J. Ma, A cost-effective electro-Fenton process with graphite felt electrode aeration for degradation of dimethyl phthalate: Enhanced generation of H<sub>2</sub>O<sub>2</sub> and iron recycling that simultaneously regenerates the electrode, *Chemical Engineering Journal*, 394 (2020) 125033.

- [57] H. Dong, B. Dong, L. Sun, Z. Chi, M. Wang, H. Yu, Electro-UV/H<sub>2</sub>O<sub>2</sub> system with RGO-modified air diffusion cathode for simulative antibiotic-manufacture effluent treatment, *Chemical Engineering Journal*, 390 (2020) 124650.
- [58] E. Mousset, L. Frunzo, G. Esposito, E.D.v. Hullebusch, N. Oturan, M.A. Oturan, A complete phenol oxidation pathway obtained during electro-Fenton treatment and validated by a kinetic model study, *Applied Catalysis B: Environmental*, 180 (2016) 189-198.
- [59] E. Mousset, S. Pontvianne, M.-N. Pons, Fate of inorganic nitrogen species under homogeneous Fenton combined with electro-oxidation/reduction treatments in synthetic solutions and reclaimed municipal wastewater, *Chemosphere*, 201 (2018) 6-12.
- [60] E. Mousset, L. Quackenbush, C. Schondek, A. Gerardin-Vergne, S. Pontvianne, S. Kmiolek, M.-N. Pons, Effect of homogeneous Fenton combined with electron transfer on the fate of inorganic chlorinated species in synthetic and reclaimed municipal wastewater, *Electrochimica Acta*, 334 (2020) 135608.
- [61] H. Dong, X. Guo, C. Yang, Z. Ouyang, Synthesis of g-C<sub>3</sub>N<sub>4</sub> by different precursors under burning explosion effect and its photocatalytic degradation for tylosin, *Applied Catalysis B: Environmental*, 230 (2018) 65-76.
- [62] X. Guo, H. Dong, T. Xia, T. Wang, H. Jia, L. Zhu, Highly efficient degradation toward tylosin in the aqueous solution by carbon spheres/g-C<sub>3</sub>N<sub>4</sub> composites under simulated sunlight irradiation, *ACS Sustainable Chemistry & Engineering*, 6 (2018) 12776-12786.
- [63] X. Su, T.A. Hatton, Electrosorption at functional interfaces: from molecular-level interactions to electrochemical cell design, *Physical Chemistry Chemical Physics*, 19 (2017) 23570-23584.
- [64] H.-D. Lim, D.H. Kim, S. Park, M.E. Lee, H.-J. Jin, S. Yu, S.H. Oh, Y.S. Yun, Magnesiophilic graphitic carbon nanosubstrate for highly efficient and fast-rechargeable Mg metal batteries, *ACS Applied Materials & Interfaces*, 11 (2019) 38754-38761.
- [65] H. Zhou, Y. Shen, J. Xi, X. Qiu, L. Chen, ZrO<sub>2</sub>-nanoparticle-modified graphite felt: Bifunctional effects on vanadium flow batteries, *ACS Applied Materials & Interfaces*, 8 (2016) 15369-15378.
- [66] C. Barchiche, C. Deslouis, D. Festy, O. Gil, P. Refait, S. Touzain, B. Tribollet, Characterization of calcareous deposits in artificial seawater by impedance techniques: 3 — deposit of CaCO<sub>3</sub> in the presence of Mg(II), *Electrochimica Acta*, 48 (2003) 1645-1654.
- [67] M. Piri, R. Arefinia, Investigation of the hydrogen evolution phenomenon on CaCO<sub>3</sub> precipitation in artificial seawater, *Desalination*, 444 (2018) 142-150.
- [68] S.M. Hoseinie, T. Shahrabi, Influence of ionic species on scaling and corrosion performance of AISI 316L rotating disk electrodes in artificial seawater, *Desalination*, 409 (2017) 32-46.
- [69] C. Gabrielli, M. Keddam, A. Khalil, R. Rosset, M. Zidoune, Study of calcium carbonate scales by electrochemical impedance spectroscopy, *Electrochimica Acta*, 42 (1997) 1207-1218.
- [70] J. Marin-Cruz, R. Cabrera-Sierra, M. Pech-Canul, I. Gonzalez, Characterization of different allotropic forms of calcium carbonate scales on carbon steel by electrochemical impedance spectroscopy, *Journal of Applied Electrochemistry*, 34 (2004) 337-343.

[71] L.A. da Silva, V.A. Alves, M.A.P. da Silva, S. Trasatti, J.F.C. Boodts, Electrochemical impedance, SEM, EDX and voltammetric study of oxygen evolution on Ir + Ti + Pt ternary-oxide electrodes in alkaline solution, *Electrochimica Acta*, 41 (1996) 1279-1285.

[72] Á.R.L. da Silva, A. Jhones dos Santos, E.V. dos Santos, D.R. da Silva, C.A. Martínez-Huitle, Theoretical and experimental study of the influence of cation–Eriochrome complexes on the BDD anodic oxidation of Eriochrome Black T solutions, *Electrochemistry Communications*, 112 (2020) 106668.

[73] A.J. dos Santos, M.D. de Lima, D.R. da Silva, S. Garcia-Segura, C.A. Martínez-Huitle, Influence of the water hardness on the performance of electro-Fenton approach: Decolorization and mineralization of Eriochrome Black T, *Electrochimica Acta*, 208 (2016) 156-163.